

A numerical investigation into the influence of bio-inspired leading-edge tubercles on the hydrodynamic performance of a benchmark ducted propeller

Callum Stark, Weichao Shi, Mehmet Atlar

**Naval Architecture, Ocean and Marine Engineering, University of Strathclyde,
Glasgow, UK**

Corresponding Author:

Weichao Shi, weichao.shi@strath.ac.uk

**Department of Naval Architecture, Ocean & Marine Engineering, University of
Strathclyde**

Henry Dyer Building, 100 Montrose Street,

Glasgow, G4 0LZ, United Kingdom

Tel: +44 (0)141 574 5349

Abstract: Marine ducted thrusters are widely used to provide propulsive thrust for a range of marine vessels due to their high thrust capability in heavy loaded conditions. This paper presents a novel and optimised bio-inspired marine ducted thruster, where leading-edge tubercles are applied to the duct of a ducted propulsor to explore the impact on hydrodynamic performance. Nine different geometrical configurations of tubercle were investigated with varying amplitude and wavelength within the optimisation study. The hydrodynamic performance of the marine ducted thruster is evaluated using a commercially available computational fluid dynamics (CFD) code, STAR-CCM+, with an incompressible implicit unsteady Reynolds-Averaged Navier Stokes (RANS) solver combined with the Body Force Propeller (BFP) method for the duct optimisation study. Then, the selected optimal duct was chosen for further analysis using the propeller resolved Rigid Body Motion (RBM) method, more commonly known as the sliding mesh technique. Through the numerical optimisation study, the leading-edge modification is predicted to have the capability to enhance the duct thrust in the heavy-loaded conditions, although this is dependent on the wavelength and amplitude of the tubercle. Furthermore, during the investigation the traditional tubercle behaviour was observed, namely the high-low pressure patterns and streamwise counter-rotating vortices. Interestingly, flow separation was observed to be compartmentalised on the outer side of the duct cross-section in conditions where flow separation occurred such as at the maximum efficiency operating point.

Keywords: Ducted propeller; CFD; Biomimetics; Humpback whale; Leading-edge tubercles

Nomenclature

$10K_Q$, Torque Coefficient

A , Amplitude, Swept Area

c , L_{DUCT} , Chord length of duct

$Coef$, coefficient

$C_{0.7R_L}$, Blade chord length at 70% blade radius

C_p , Static pressure coefficient

C_T , Thrust loading coefficient

D , Propeller diameter

ETA , Propulsive efficiency

F_{bx} , Axial body force

$F_{b\theta}$, Tangential body force

J , Advance ratio

K_{TD} , Duct thrust coefficient

K_{TP} , Propeller thrust coefficient

K_{TT} , Total thrust coefficient

n , Propeller revolutions per second

P_0 , Static pressure

P -value, measures the significance of variable on response

Q , Torque

R -sq, coefficient of determination

R -sq(adj), adjusted coefficient of determination

Re , Reynolds Number

R_H , Inner (hub) radius

R_T , Outer (blade tip) radius

S , standard deviation

SE $Coef$, standard error of the coefficient

T -Value, ratio between the coefficient and its standard error

T_D , Duct thrust

T_P , Propeller thrust

VIF , variance inflation factor

V_A , Advance velocity

y^+ , non-dimensional distance from the wall to the first mesh node

β , Number of tubercles

Δ , Virtual disk thickness

λ , Tubercle wavelength

ρ , Density

1 Introduction

Improving the performance of propulsive device is a continuous challenge and even more so particularly now with the pressure of tackling climate change over the shipping industry. With enforcement of the Energy Efficiency Design Index (EEDI), the desires for energy saving and emission reduction is necessary in the marine industry. However, the energy saving devices (ESDs) are highly focused on ocean-going vessels for transportation whereas tugboats, fishing vessels, submersibles and operational vehicles are left behind. These vessels have a highly versatile operation profile requiring them to be able to perform in various operating conditions but, currently the propulsion systems are all optimised towards a single target, which means performance degradation in off-design conditions.

Meanwhile for these vessels, ducted propulsors are widely adopted since an enhanced thrust capability can be produced in the bollard pull condition due to the contribution of the duct thrust, the thrust is the horizontal net force comprising of the horizontal lift component and drag. This creates additional thrust to the overall propulsor, where the acceleration of fluid through the duct due to the propeller creates a pressure difference between suction and pressure sides of the cross-sectional profile. On the other hand, a ducted thruster can provide similar propulsion efficiency while reducing radiated noise levels due to the duct enclosure, which is beneficial to the marine acoustic environment while meeting the EEDI regulations. However, this comes with a penalty of duct drag/reduced thrust while in transit condition comparing to the open propellers.

To solve these issues, one can look to nature for inspiration. The humpback whale (*Megaptera novaeangliae*) is an exceptional marine mammal, undertaking acrobatic manoeuvres to catch prey despite its stocky build. Such manoeuvres are assisted by leading edge tubercles, which are bumps or perturbations located on the pectoral fin and as a result are the topic of extensive research on a multitude of applications in a variety of industries.

Inspired by this concept, Watts and Fish., (2001) conducted initial numerical research on leading-edge (LE) tubercle modified aerofoils using Computational Fluid Dynamics (CFD). It was shown that there was performance enhancement whereby there was an increase of 17.6% in the lift to drag ratio, a 4.8% increase in lift and a 10.9% reduction in drag at 10 degrees angle of attack. The reduction in drag was believed to be due to the compartmentalisation of lift between the troughs. Miklosovic *et al.*, (2004) conducted initial experimental research on LE tubercles, this was performed in a wind tunnel test on a scale model of an idealised Humpback

whale flipper. It was shown that when compared to a smooth flipper, the LE tubercles delayed the stall angle by 40% whilst simultaneously increasing lift and reducing drag. The tubercles were hypothesised to be similar to vortex generators, which re-energize flow along the boundary layer and prolong the attachment of flow which ultimately delays stall.

Since initial findings in the early 21st century, LE tubercles have been researched on a variety of devices applicable in an array of industries such as; marine, where they have been investigated on propellers (Ibrahim and New, 2015) and hydrofoils (Johari *et al.*, 2007; Stanway, 2008); aviation, where the wing (Hansen *et al.*, 2011; Hansen *et al.*, 2012) and propeller (Butt and Talha, 2019) components have been of particular interest; and energy, where wind (Ibrahim *et al.*, 2015) and tidal turbines (Shi *et al.*, 2016; 2017) have also been benefactors of LE tubercle research.

Johari *et al.*, (2007) conducted experimental research on 2D hydrofoils in a water tunnel on leading-edge tubercles at high Reynolds number while varying the amplitude and wavelength of the idealised sinusoidal waveform. It was noted that post-stall life increased up to 50% with only ever a slight compromise in induced drag. Additionally, there was an increase in drag and reduction in lift in the pre-stall region. In terms of the sinusoidal geometrical parameters, it was shown that amplitude had a much more significant effect on the performance of the hydrofoil compared to the wavelength, which had very little. Hansen *et al.*, (2011) conducted a similar experimental research in a wind tunnel at a lower Reynolds number to investigate the effect of wavelength and amplitude on the aerodynamic performance of aerofoils. Similarly to Johari *et al.*, (2007), it was shown that amplitude had a significant impact on the aerofoil performance. But, the wavelength also had a significant impact on the performance through the optimisation of the waveform parameters. Through force visualisation, it was speculated that the LE tubercles behave similarly to counter-rotating vortex generators.

Marine control surfaces such as rudders have also been the benefactors of LE tubercle research. Weber *et al.*, (2010) used experimental methods to investigate the effect of LE tubercles on the lift, drag and cavitation onset operating at low Reynold's numbers. It was concluded that the inclusion of LE tubercles accelerated the onset of cavitation. At angles of between 15 and 22 degrees in the lower Reynolds numbers, LE tubercles increased drag and reduced lift, but at angles of above 22 degrees, the LE tubercles improved the lift capability of the rudder. At the higher Reynolds numbers, the difference in performance between the smooth LE and tubercle LE was negligible, therefore suggesting there is a critical Reynold's number to which a LE tubercle configuration can affect the hydrodynamic performance. More recently, Wei *et al.*,

(2015) conducted an experimental investigation into the influence of LE tubercles on hydrofoils at low Reynolds number, with particular focus on the flow field using particle image velocimetry (PIV). It was confirmed that LE tubercles act as vortex generators and improved the flow separation behaviour of the hydrofoil. Troll et al., (2021) used CFD to show that tubercle-induced streamwise vortices disrupted the dominant tip vortex structure which led to the acceleration in the dissipation of the tip vortex when compared to the baseline design.

The effect of LE tubercles on the hydrodynamic performance of rotating components such as propellers and turbines have also been investigated. Shi *et al.*, (2016) studied experimentally in a cavitation tunnel the effect of LE tubercles on tidal turbines. It was concluded that the LE tubercle tidal turbines had higher power coefficients in stall region operating conditions compared to a smooth LE tidal turbine. Ibrahim and New., (2015) conducted a numerical investigation into LE tubercles and their effect on the performance on marine propellers. It was shown under certain operating conditions that the thrust coefficient could be increased by 10% compared to a smooth LE bladed propeller. However, there was also an increase in torque coefficient of 10% which resulted in a decrease in net efficiency. Stark and Shi., (2021a) used CFD to show that tubercles can create a cavitation fencing pattern, which can reduce the sheet cavitation present on the propeller blades and improve hydrodynamic efficiency of the propulsor under heavy-cavitating conditions.

Inspired by the above research, there is a scope to research the application on the marine duct, since it also has potential for improvement in efficiency which is highly related to the lift and drag that can be produced in high angles of attack or highly loaded conditions. Therefore, this research has been initiated. In this paper, the research has been conducted to study the best effective approach to apply LE tubercles on a benchmarked marine duct, the 19A duct. Supported by the numerical simulation and optimisation, the designs of the LE tubercles have been comprehensively studied with a range of tubercle designs investigated. The study has been initiated to understand the effect on the global hydrodynamic performance of ducted propellers as well as fundamental fluid dynamics such as pressure, velocity and vorticity distributions. This was achieved by firstly exploring a variety of different amplitude and wavelength configurations economically using inexpensive simplified actuator disk modelling to represent the propeller to find an optimised design in terms of hydrodynamic performance at key conditions. Then, further analysis using a propeller resolved modelling technique was conducted to understand the influence of LE tubercles in a more realistic setting in a larger range of operating conditions.

The paper is structured as the following: Section 2 will firstly describe the baseline and sinusoidal leading-edge (SLE) ducted propeller geometry. The numerical methodology will then be outlined in Section 3, describing the computational domain, the propulsive efficiency quantification method where the benchmark experimental data for validation of the numerical modelling will be presented and finally, the specific actuator disk modelling and propeller resolved methods to represent the propeller within the CFD solver. Section 4 describes the verification and validation study. The verification methodology and results of the mesh study is presented, using the grid convergency index (Celik *et al.*, 2008) as the criteria for mesh convergence. The numerical results of both methodologies of the baseline geometry over a range of operating conditions is then validated with available experimental data. Section 5 presents the results and analysis of the sinusoidal leading-edge (SLE) tubercle duct optimisation using the simplified actuator disk modelling, where a number of duct designs with varying amplitude, A and wavelength, λ configurations are analysed systematically. The pressure distribution and streamwise vorticity on the duct surface are discussed. An optimal SLE duct is then selected for further analysis in Section 6 using the propeller resolved method, with the investigation conducted over a wide range of operating conditions with a discussion on the propeller inflow characteristics, pressure, velocity and vorticity distributions. The paper concludes with some final remarks and the author's planned future work.

2 Ducted Propeller Modelling

In this study, a widely available marine ducted propulsion system has been selected to perform the study. Figure 1 depicts the selected open-access baseline design of a KA4-55 propeller (Kaplan Propeller) and a benchmark 19A duct used in both propeller resolved and actuator disk, body force propeller (BFP) methodologies (Carlton, 2018). The ducted propulsor combination has been previously tested in an internal test campaign conducted in CTO, Poland. Table 1 describes the main geometrical parameters of the baseline model-scale duct and propeller.

With the above 19A duct as the reference, the LE modified duct was modelled and named the sinusoidal shaped LE tubercle (SLE) duct. To model the LE modified ducts, tubercle profiles were created along an arc to create a guideline. This guideline was used to guide the surface loft of the leading-edge modification, and this required three equations as a function of t with a start and end parameter to control the cartesian coordinates (x_t, y_t, z_t) . The starting point was the upright point at the leading edge of the duct $(0,150,0)$ mm:

For SLE, the sinusoidal curve is defined as in Equation 1.

$$x_t = A \sin(\beta t) - A \quad (1)$$

To create the circular arc profile to which the sinusoidal curve is constrained along, the equations are defined as in Equation 2 and 3:

$$y_t = 150 \sin(t) \quad (2)$$

$$z_t = 150 \cos(t) \quad (3)$$

The equation to define the start and end parameter to create the circle is shown in Equation 4.

$$t_1, t_2 = (0, 2\pi) \quad (4)$$

Where A is the amplitude of tubercles, mm and β is the number of tubercles which can be calculated from the selected wavelength, mm.

Figure 2 illustrates the SLE waveform implemented as modifications on the reference design. 10 models were created for the parametric optimisation investigation and are shown in Table 2 where the amplitude and wavelength were varied. Figure 3 shows the parametric family of tubercle wavelength and amplitude configurations.

3 Numerical Simulation Methodology

Computational Fluid Dynamics (CFD) was used to predict the hydrodynamic performance of both the 19A and LE modified ducts using commercial software STAR-CCM+. Firstly, an actuator disk model was implemented using the body force propeller (BFP) method which allowed the propeller thrust and torque to be maintained the same while isolating the variables only to the duct. The rotation rate was fixed at 15rps and advance velocity, V_A varied as according to the experimental setup.

In both methodologies, implicit unsteady incompressible Reynolds-Averaged Navier Stokes (URANS) was implemented with the SST K-Omega turbulence model. The convective and temporal terms in the momentum equations were discretised with a 2nd order scheme. The equations were coupled by using a segregated SIMPLE type solution algorithm. Low y^+ wall treatment was used with $y^+ < 1$ and this was achieved by applying prismatic cells in the duct boundary layer.

Using the actuator disk modelling, a time-step of 0.001 was selected, while the propeller thrust and torque were kept constant with time. Polyhedral mesh was used for the domain as it is estimated to require four times fewer cells, half the memory and a tenth to fifth of computing time compared to tetrahedral meshes to reach solutions of the same accuracy. As solution time and memory were of critical importance during the optimisation process, this was the reason for selection.

The selected optimised duct was further analysed using the Rigid Body Motion (RBM) method, known as the sliding mesh technique, to describe the propeller rotation and predict the key hydrodynamic variables of the optimised design. A time-step of 1 degree of rotation per time step was used, approximately $1.85e^{-4}s$, a time-step of between 0.5 and 2 degrees is recommended by ITTC (ITTC, 2014). Unstructured hexahedral mesh constituted the domain with previous literature showing excellent predictions with experimental data (Sezen *et al.*, 2020).

3.1 Computational Domain and Mesh Generation

3.1.1 Actuator Disk Modelling (BFP Method)

Figure 4 depicts the definition of computational domain and its associated boundary conditions. The boundary conditions were selected as velocity inlet on the left face, pressure outlet on the right face, and a symmetry plane on the cylindrical revolving face. The velocity magnitude at the velocity inlet was altered to vary the advance ratio, J . The pressure outlet was defined as 0 Pascal with respect to the reference pressure. The duct was modelled as a non-slip wall boundary. Computational domain dimensions are taken from the propeller plane and are as follows: 3D upstream to the velocity inlet, 7D downstream to the pressure outlet and a radius of 2.5D.

Two volumetric controls were created to ensure a high-quality mesh surrounding the duct, especially in the downstream direction to capture the turbulent wake structure accurately and can be shown in Figure 5, resulting in a final mesh count of approximately 8 million cells. Figure 6 shows the reference duct surface mesh using in the study.

3.1.2 Propeller Resolved Method

Using the propeller resolved method, the computational domain consisted of a cylindrical domain, where the propeller was located 3D from the inlet and 8D from the outlet and 2.5D from the outer circumferential wall. The inlet was defined as a velocity inlet, outlet as pressure outlet (0 Pascal) and symmetry plane on the circumferential face as shown in Figure 7. A

rotating region was defined to rotate the propeller, while the surrounding region was defined as static. An interface between both regions was created to ensure mesh alignment of the cells. The duct and propeller were defined as no-slip walls. The total mesh count was around 13 million cells. A plane cut section of the volume mesh can be shown in Figure 8, and blade and duct surface mesh shown in Figure 9.

3.2 Propulsive Efficiency Quantification Methodology

In order to assess the hydrodynamic performance of each duct, the open water characteristics need to be quantified. This follows the traditional propulsive efficiency analysis method. The following nondimensional parameters are used. The advance ratio, J , is defined in the following Equation 5.

$$J = \frac{V_A}{nD} \quad (5)$$

where, n [rps] is the rotation rate; D [m] is the diameter of propeller; and V_A [m/s] is the advance velocity.

For each advance ratio, the propeller and duct thrust coefficients, K_{TP} and K_{TD} are calculated in Equation 6 and 7, respectively.

$$K_{TP} = \frac{T_P}{\rho n^2 D^4} \quad (6)$$

$$K_{TD} = \frac{T_D}{\rho n^2 D^4} \quad (7)$$

Where T_P [N] and T_D [N] is the propeller and duct thrust, respectively; and ρ [kg/m³] is density,

The total thrust coefficient from the propeller and duct combination, K_{TT} , is defined in Equation 8,

$$K_{TT} = K_{TP} + K_{TD} \quad (8)$$

The torque coefficient, K_Q , is defined as in Equation 9, where Q [Nm], is propeller torque,

$$K_Q = \frac{Q}{\rho n^2 D^5} \quad (9)$$

Hydrodynamic efficiency, ETA , is defined as in Equation 10,

$$ETA = \frac{J}{2\pi} \frac{K_{TT}}{K_Q} \quad (10)$$

Once the hydrodynamic efficiency is known for each advance ratio, an open water characteristic diagram can be plotted.

Additionally, the thrust loading coefficient, C_t , can be calculated as follows in Equation 11,

$$C_t = \frac{T_D + T_P}{\frac{1}{2}\rho V_A^2 A} \quad (11)$$

Where area, A [m²], is calculated based on the propeller swept area.

The representative Reynolds number, Re , can be calculated as shown in Equation 12.

$$Re = \frac{C_{0.7r} \sqrt{V_A^2 + (0.7\omega r)^2}}{\nu} \quad (12)$$

Where $C_{0.7r}$ [m], is the chord length of the blade at $0.7r$, ω [rad/s], is rotational rate of the propeller, r [m] is propeller radius and ν [m²/s], is kinematic viscosity.

The experimental open water characteristics of the duct and propeller combination were evaluated in CTO and Figure 10 illustrates the experimental open water characteristic curve for the KA4-55 propeller and 19A duct. For the evaluated cases, the Reynolds number (Re) can be calculated for each advance ratio and is tabulated in Table 3.

3.3 The Body Force Propeller (BFP) Method

The actuator disk model and the BFP method was selected for the duct optimisation as it allowed the thrust and torque produced from the propeller to be maintained, thus isolating the duct performance.

The BFP method is available through the commercial software STAR-CCM+. It simplifies the propeller to an actuator disk and requires the following fundamental steps in order to successfully implement it. The BFP method employs a uniform volume force distribution over the cylindrical virtual disk, but the volume force varies in the radial direction, this radial distribution can be defined by the user. Firstly, the position and direction in which thrust is produced are considered. In this case, the position of the virtual disk was placed at 50% duct chord length ($0.5L_{DUCT}$) as per experimental setup conducted by Miller and Grzybowski., (2007) and the direction of thrust was in the opposite direction to the advance velocity. Then, the open water propeller performance curve of the specific propeller to be simulated are

specified. In this case, this was a 4 bladed Kaplan series propeller with an expanded blade area ratio of 0.55, where the performance curve was acquired experimentally by Miller and Grzybowski., (2007). Then, the operating point was specified and in this case was the rotational speed and the advance ratio was varied by varying the advance velocity. The inflow method was selected as velocity inflow boundary and the boundary selected was the inlet. A summary of the virtual disk parameters selected can be shown in Table 4.

The radial distribution of thrust and torque can be defined by the Goldstein's Optimum Distribution (Reissner., 1937) through user-based field function or as the default option, which can be calculated as described herein and can be found within the STAR CCM+ user guide (STAR CCM+, 2018). The BFP method employs a uniform volume force $f_b [N]$, distribution over the cylindrical virtual disk. The volume force varies in the radial direction, which is defined by the Goldstein's Optimum Distribution as default. The distribution can be calculated as in Eqns. 13-18:

$$f_{bx} = A_x r^* (1 - r^*)^{0.5} \quad (13)$$

$$f_{b\theta} = A_\theta r^* \frac{(1 - r^*)^{0.5}}{r^* (1 - r'_h) + r'_h} \quad (14)$$

$$r^* = \frac{(r' - r'_h)}{(1 - r'_h)} \quad (15)$$

$$r^* = \frac{(r' - r'_h)}{(1 - r'_h)} \quad (16)$$

$$r'_h = \frac{R_H}{R_P} \quad (17)$$

$$r' = \frac{r}{R_P} \quad (18)$$

Where, $f_{bx} [N]$ is the body force in the axial direction, $f_{b\theta} [N]$ is the body force in the tangential direction, $r [m]$ is the radial coordinate, $R_H [m]$ is hub radius and $R_P [m]$ is the tip radius from the propeller centre. The constants A_x and A_θ can be calculated as in Eqns. 19-20, respectively.

$$A_x = \frac{105}{8} \frac{T_p}{\pi \Delta (3R_H + 4R_P)(R_P - R_H)} \quad (19)$$

$$A_\theta = \frac{105}{8} \frac{Q}{\pi \Delta R_P (3R_H + 4R_P)(R_P - R_H)} \quad (20)$$

Where Δ [m] is the virtual disk thickness. Therefore, Goldstein's Optimum Distribution of thrust and torque can be plotted against normalised span disk span r^* . Two radial distributions for axial (thrust) and tangential (torque) forces are developed inhouse based on Goldstein's Optimum Distribution, with Eqn.21 and 22 for heavy loading condition ($0 \leq J \leq 0.4$) and Eqn. 23 and 24 for lightly loaded condition ($0.4 < J \leq 0.7$). The graphic illustration of the radial distributions can be shown in Figure 11. As can be shown, the location of the maximum axial force (thrust) has been shifted from 67% of the blade radius, to approximately 77% for lightly-loaded condition, $0.4 < J \leq 0.7$ and 83% for heavy-loaded conditions, $0 \leq J \leq 0.4$. In addition, the degradation of axial body force from the maximum point to the blade tip has been reduced with the author-modified distributions. This is typical of a duct application as the 3D effect due to the suppression of a fully-developed tip vortex is reduced when compared to open rotating machinery. The Goldstein's Optimum Distribution was formulated for open rotating applications as oppose to duct applications, therefore this is the reason for the modifications.

$$f_{bx} = A_x r^* (1 - r^*)^{0.2} \quad (21)$$

$$f_{b\theta} = A_\theta r^* \frac{(1 - r^*)^{0.2}}{r^* (1 - r'_h) + r'_h} \quad (22)$$

$$f_{bx} = A_x r^* (1 - r^*)^{0.3} \quad (23)$$

$$f_{b\theta} = A_\theta r^* \frac{(1 - r^*)^{0.3}}{r^* (1 - r'_h) + r'_h} \quad (24)$$

4 Verification and Validation Study

4.1 Mesh Convergence Study

A verification study was conducted to determine the uncertainty of the numerical simulations. This was completed using the grid convergence (GCI) method first proposed by (Roache, 1998) and based on (Richardson, 1911). Additionally, this method is also recommended in the ITTC procedure (ITTC, 1999). The full methodology implemented in this study was defined by Celik et al (Celik *et al.*, 2008). As propeller torque and thrust coefficients were kept constant during

this investigation, the duct thrust coefficient K_{TD} was selected as the integral variable for the BFP method. K_{TT} and $10K_Q$ were selected for the propeller resolved method using a steady RANS moving reference frame (MRF) approach to save computational time. Both studies were completed at $J = 0.55$, the maximum operating efficiency point.

The difference between the solution scalars (ε) should be determined by Eqn. 25.

$$\varepsilon_{21} = \varphi_2 - \varphi_1, \quad \varepsilon_{32} = \varphi_3 - \varphi_2, \quad (25)$$

where, φ_1 , φ_2 and φ_3 represent the results using fine, medium and coarse mesh grids, respectively. The ratio of solution scalars is used to calculate the convergence condition by Eqn. 26.

$$R = \frac{\varepsilon_{21}}{\varepsilon_{32}} \quad (26)$$

Solution type is determined with respect to the convergence condition, R : 1. oscillatory convergence, $-1 < R < 0$; 2. monotonic convergence $0 < R < 1$; 3. oscillatory divergence $R < -1$; and 4. monotonic divergence, $R > 1$, If R is found as in case 2, the procedure can be directly employed. GCI index is calculated by the following in Eqn. 27:

$$GCI_{fine}^{21} = \frac{1.25e_a^{21}}{r_{21}^p - 1} \quad (27)$$

Here, p is apparent order, e_a is an approximate relative error. e_a can be calculated as in Eqn. 28 and r_{21} , grid refinement factor between the medium and fine mesh can be calculated as defined in Eqn. 29. The grid refinement factor used was above 1.3 for both methodologies, where the recommendation is a value of above 1.3 by Celik et al., (2008).

$$e_a^{21} = \left| \frac{\varphi_1 - \varphi_2}{\varphi_1} \right| \quad (28)$$

$$r_{21} = \frac{h_2}{h_1} \quad (29)$$

Where h_1 and h_2 are the representative cell sizes for fine and medium grid structures.

Detailed information about the verification procedure can be found in (Celik et al., 2008). Results obtained for the duct thrust coefficient and uncertainty level using the BFP method and total thrust and torque coefficient results and uncertainty levels using the propeller resolved method are given in Table 5. As can be shown, the convergence condition (R) was between 0

and 1 (monotonic convergence) for both the BFP and propeller resolved methods and each key independent variable. As a result of the uncertainty study at $J=0.55$, the fine mesh was selected for each method. The same grid structure was then applied for all case studies, although this grid structure differed for both actuator disk and propeller resolved methodologies.

4.2 Hydrodynamic Validation against the Experimental Test

The validation was done by comparing experimental data acquired by Miller and Grzybowski., (2007). Figure 12 shows the results acquired using the BFP method, where advance ratios ranging from 0.001 to 0.7 were considered. The comparison between CFD and the experimental data is made between the duct thrust and overall efficiency as the experimental propeller torque (K_Q) and thrust (K_{TP}) coefficients are used as inputs, which can be seen defined in Figure 12. From this validation study, it can be observed that the developed method can accurately predict the duct thrust and the results matched well with the experimental results. In addition, the results acquired using the propeller resolved method with a steady MRF approach can be shown in Figure 13 and compared to the same experimental data. As can be seen in Figure 13, the computational environment generated can be used to determine the open water characteristics of the ducted propeller selected in this study to within a good degree of accuracy, with relative errors of total thrust and torque coefficient; 5.1 and 1.4% respectively.

5 Results and Discussion using BFP Method

5.1 Optimisation of Duct Hydrodynamic Performance

The bollard pull condition and the maximum efficiency operating condition, with advance ratios $J = 0.001$ and 0.55 were considered to investigate the effect of geometrical parameter variations on the SLE tubercle duct. At $J = 0.001$, the duct experiences a high negative angle of attack, however at $J = 0.55$, the inflow angle is much more modest as can be seen from Figure 14. Through conducting the above demonstrated CFD simulations, the hydrodynamic results in terms of the propulsive indicators can be extracted and summarised as shown in Table 6. At $J = 0.001$, the duct thrust coefficient can be correlated to the varying wavelength and amplitude as a function of chord length, c , which is equal to L_{DUCT} . In the bollard pull condition, the following general trend can be observed. First, while maintaining constant wavelength, a reduction in amplitude results in an increase in duct thrust performance. Second, while maintaining the amplitude, increasing the wavelength also results in an improvement of duct thrust performance in all cases. Therefore, in the current range of optimisation for the bollard

pull condition, the simulation results indicate smaller amplitude and larger wavelength to be favourable, which directs the optimisation to the reference design with $A=0$ and $\lambda = +\infty$. The trend is monotonic and ends in 5A_10F, which shows to be the optimum design. Further extending the optimisation range is feasible numerically but the tubercle feature became less noticeable. But between the tubercle duct and the reference duct, the design did show a noticeable improvement.

On the other hand, at $J = 0.55$, the duct performance is not very sensitive to the varying amplitude and wavelength. It is noted that there is a limited change to duct thrust, therefore the later optimisation is focused on the bollard pull condition.

Following on general trend observation, a further regression analysis was conducted for both operating points to statistically interpret the impact of variables wavelength and amplitude on the response, duct thrust coefficient and to fit a model to predict the response at different configurations. The regression equation fitted to the optimisation data set for $J = 0.001$ was as shown in Eqn. 30 with Table 7 and Table 8 showing the regression analysis uncoded coefficients and model summary, respectively.

$$K_{TD} = 0.22754 - 1.026\frac{A}{c} - 0.1192\frac{\lambda}{c} + 1.83\left(\frac{A}{c}\right)^2 + 0.0852\left(\frac{\lambda}{c}\right)^2 - 0.155\left(\frac{A}{c}\right)\left(\frac{\lambda}{c}\right) \quad (30)$$

The regression equation fitted to the optimisation data set for $J = 0.55$ was as shown in Eqn. 31 with Table 9 and Table 10 showing the regression analysis uncoded coefficients and model summary, respectively.

$$K_{TD} = 0.02603 - 0.0186\frac{A}{c} - 0.00408\frac{\lambda}{c} + 0.354\left(\frac{A}{c}\right)^2 + 0.00572\left(\frac{\lambda}{c}\right)^2 - 0.0563\left(\frac{A}{c}\right)\left(\frac{\lambda}{c}\right) \quad (31)$$

A p-value lower than 0.05 indicates that the variable is statistically significant and therefore both predictor variables - wavelength and amplitude at $J = 0.001$ are statistically significant on the response, duct thrust coefficient as shown in Table 7. Additionally at $J = 0.001$, the variation in amplitude resulted in a larger impact on response variable, duct thrust, comparing to the wavelength which agrees with previous optimisation studies on hydrofoils in the pre-stall regime (Johari *et al.*, 2007). But, as observed in the optimisation, the wavelength also has a non-negligible impact on the duct thrust. At $J = 0.55$, it was not determined if wavelength and amplitude were statistically as shown in Table 9.

As can be shown in Figure 15, the surface plot predicts the optimal duct performance at low amplitude, high wavelength configuration, 5A_10F, at $J = 0.001$. Figure 16 shows the surface plot at $J = 0.55$, showing the low amplitude high wavelength configuration, 5A_10F, to be one of the top performers at this condition although the variation in results at this condition is small. Based on the simulation results, it is observed that 5A_10F shows the highest duct thrust improvement over the operational envelope which consists of an $A = 0.08L_{DUCT}$ and $\lambda = 0.75L_{DUCT}$. This finding shows that leading-edge tubercle design favours large but mild candidates, which have capacity to energise the vortex flow but do not consume too much energy in generating these secondary vortices.

5.2 Surface Pressure Distributions

Figure 17 and Figure 18 illustrates the scalar plot of the pressure distribution on the reference and SLE ducts, 5A_10F, 10A_10F, 10A_20F at operating conditions $J = 0.001$ and 0.55 respectively. At the heavy-loaded condition, the influence of the tubercles can be shown clearly with high to low pressure pattern observed on the suction side of the duct from peak to trough, respectively. In the heavy-loaded condition the tubercle peak experiences increased pressure behind the peaks with increasing amplitude and reducing wavelength. However, this increase in amplitude or reducing wavelength resulted in a degradation in duct thrust performance when comparing 5A_10F to the other SLE ducts at $J = 0.001$. The degradation in duct thrust performance can also be related to the increasing steepness of the tubercle (A/λ). The improvement in duct thrust can be further confirmed by comparing 2D static pressure coefficient plots between REF and SLE, 5A_10F duct in Figure 19a, where the inclusion of tubercles induces a larger low-pressure region behind the tubercle trough on the inner duct section when compared to the REF design and the addition of a peak which increases the surface area where a useful pressure gradient between outer and inner duct boundaries can be obtained, resulting in an improved lift and therefore, thrust for the optimised configuration. The static pressure coefficient, C_p , can be defined as in Eqn. 32, where P_0 [Pa], is static pressure.

$$C_p = \frac{P_0}{0.5\rho V_A^2} \quad (32)$$

At the lightly-loaded condition $J = 0.55$, the variation in surface pressure distribution on the suction side of the duct is minimal. The 2D static pressure coefficient plots are shown in Figure 19b.

5.3 Vorticity Distribution and the Turbulent Wake Structure

Figure 20 and Figure 21 shows the SLE tubercle ducts 5A_10F, 10A_10F and 10A_20F streamwise vorticity on the duct surface at $J=0.001$ and 0.55 , respectively. As can be seen, the number of counter-rotating pairs is directly proportional to the tubercle count within the configuration. At $J = 0.001$ and 0.55 , an increase in amplitude and a reduction in wavelength results in an increase in counter-rotating vortex strength on the suction side of the duct cross-section. At $J = 0.55$, the vortex pairs can be visible on the pressure side of the duct, which increase in strength with an increase in amplitude and reduction in wavelength, although an increase in amplitude has a larger impact on vortex pair strength when compared to wavelength. As amplitude is increased and wavelength is reduced, the steepness of the tubercle, A/λ ratio increases. Therefore, the advance ratio, J , A , λ and the A/λ ratio of the tubercle will influence the induced vortex pairs.

From Figure 22, it is interesting to note that the petal-shaped vortex pattern can be observed clearly and there is a marginal reduction in maximum vorticity strength for all SLE ducts when compared to the reference duct, although the vortex structure spans over a larger area.

Figure 23 illustrates the vorticity magnitude in the streamwise direction at $X/D = 0.6, 1.2$ and 1.5 from the duct entrance for the LE modified (5A_10F) and reference duct at the optimum operating efficiency point. As can be seen, the LE tubercle duct disrupts the typical ring vortex structure from the reference design.

Based on the above simulations, the SLE, 5A_10F duct was selected for further investigation due to the improvement in performance at the heaviest-loaded condition. This was conducted by replacing the actuator disk with a physical propeller model to understand the resulting influence of the LE tubercles on key propeller performance characteristics such as blade thrust and torque which will affect the final propulsive efficiency.

6 Results and Discussion using Propeller Resolved Method

6.1 Global Hydrodynamic Performance Results and Analysis

Through the optimisation study, the SLE (5A_10F) duct can be seen to show favourable performance in both operating conditions considered when compared to the alternative designs. Therefore, further analysis was conducted on the SLE (5A_10F) duct using a propeller resolved method. Although the actuator disk modelling provided an inexpensive environment to perform the optimisation study efficiently, it is a simplified environment and does not take into account

the effect tubercles will incur on the propeller, therefore using the propeller resolved method will shed light on such effects. The difference in performance variables due to the inclusion of LE tubercles can be shown for a variety of J in Figure 24. Generally, there is a good agreement between both methods in terms of duct thrust as it is enhanced at the heaviest loaded conditions and then there is a performance degradation in the lightly loaded conditions, similar to the previous results using the BFP method. The difference in performance prediction between both methods is due to the propeller resolved method including the physical propeller, which will predict the tip leakage vortex, the resulting difference in pressure distributions on the duct which will arise from this and, the tubercle's influence on other key performance variables such as propeller thrust and torque, which will affect the final propulsive efficiency.

The propulsive efficiency, ETA , vs. total thrust coefficient, C_t , for both ducted propeller combinations can be compared in Figure 25. Although there is an improvement in the duct thrust performance at the heavier-loaded conditions, the resulting reduction in propeller thrust results in a lower thrust coefficient at each J , but, as there is also a reduction in torque, the propulsive efficiency is increased. Therefore, at the same efficiency, the total thrust coefficient, C_t , is very similar.

6.2 Plane Section Inside Duct Hydrodynamic Characteristics

As was noted in the global hydrodynamic performance, the inclusion of the LE tubercles reduce the propeller performance characteristics thrust and torque. Therefore, the inflow characteristics must be affected by the LE tubercles inside the duct. Figure 26 show the inflow pressure, velocity and streamwise vorticity characteristics taken at $0.26L_{DUCT}$ for operating condition $J = 0.3$. As can be seen, although there is no appreciable difference in velocity or pressure distributions at this cross-section, the streamwise-vortices produced by the tubercles can be observed.

6.3 Pressure, Vorticity and Velocity Distributions

Figure 27 - Figure 28 show the surface pressure distributions of REF and SLE (5A_10F) duct for $J = 0.1, 0.3$ and 0.55 at both propeller suction and pressure sides, respectively. The inclusion of the physical propeller results in the tip leakage vortex to be predicted, which can be illustrated by the sharp pitching low pressure line around the mid-point of the duct and this effects the pressure distribution on the duct surface. This is the reason for the slight difference in performance results between the two methods as the BFP method simulates the propeller as a disk and thus, there are no blades within that environment.

Figure 29 shows the surface streamwise vorticity distributions of REF and SLE (5A_10F) duct for $J = 0.1, 0.3$ and 0.55 . The results are in good agreement with the BFP method, where similar streamwise vorticity can be shown for the SLE (5A_10F) duct and a vortex pair can be shown on the pressure side of $J = 0.55$. The tip leakage vortex can be observed for both configurations on the suction side of the duct at $0.5L_{DUCT}$.

Figure 30 shows the velocity streamlines on the outer side of both REF and SLE duct, which shows that flow-separation is induced earlier behind the troughs of the SLE duct when compared to the REF duct which is the reason for the reduction in the thrust at the higher J 's.

7 Conclusions

As demonstrated in this paper, pioneering research has been conducted to research the application of leading-edge tubercles and the influence of varying geometrical configurations of amplitude and wavelength on the duct of a benchmark ducted propeller using both simplified actuator disk modelling and propeller resolved computational methods coupled with the RANS-based solver for the first time. With the numerical simulations, the following main conclusions can be drawn:

A novel design concept has been presented in terms of the leading-edge tubercle (SLE) as applied on the ducted propeller, where it has been shown that there are potential benefits in hydrodynamic performance where maximum duct thrust capability can be enhanced. However, the propeller thrust and torque were reduced at each operating condition. Where flow-separation occurs on the outer side of the duct ($J \geq 0.5$), the tubercles can be shown to compartmentalise the flow separation and isolate the stall to the troughs of the tubercles.

Through completion of the optimisation process, it is evident that the optimum tubercle wavelength and amplitude combination is application dependant as they affect the operating conditions studied differently. The LE tubercle configuration small amplitude and larger wavelength configuration, $A = 0.08L_{DUCT}$ and $\lambda = 0.75L_{DUCT}$, provided the best compromise at the key operating conditions considered. It was noted that both amplitude and wavelength had an impact on the duct thrust at $J = 0.001$. As amplitude was reduced and wavelength kept constant, an improvement in duct thrust was predicted while increasing wavelength and maintaining amplitude resulted in an improvement in duct thrust. The change in amplitude had a more significant impact on the duct thrust than the change in wavelength. At $J = 0.55$, all tubercle models predicted a degradation in duct thrust performance due to the influence on the

flow-separation behaviour of the duct, but this needs to be further analysed using scale-resolved methods such as Detached Eddy Simulations (DES). This is because the suitability of RANS to accurately capture and predict the complex flow phenomena induced by tubercles and the resulting performance variables such as lift and drag, particularly in flow separation conditions (which occur above $J = 0.5$) have been questioned (Weber *et al.*, 2011). Also, RANS-based methods cannot capture the instabilities within the propeller slipstream (Guilmineau *et al.*, 2014). Nonetheless, both methodologies implemented within this study coupled with the RANS solver have provided initial insights into the impact of LE tubercles on the fundamental fluid dynamics on the benchmark ducted propulsor that should be further investigated using high-fidelity computational modelling.

The key findings listed above naturally lead to a set of recommendations for future work in this topical area to extend impact of LE tubercle modifications on ducted marine propellers. This work could benefit from the use of more high-fidelity computational modelling using DES. In addition, the hydroacoustic performance of the SLE duct would be interesting to investigate further, as tubercles have shown to provide noise reduction capabilities and reducing anthropogenic contributions to underwater radiated noise from marine craft is also a critical issue to tackle alongside carbon emissions within the industry. This study has been initiated by Stark and Shi., (2021b), where the influence of tubercles on the vortex dynamics in the ducted propeller slipstream have been investigated using the DES method. A model-scale test campaign would provide further validation of the findings presented within the paper. This is the author's planned future work.

Acknowledgements

Results were obtained using the ARCHIE-WeST High-Performance Computer (www.archie-west.ac.uk) based at the University of Strathclyde. The funding support from BAE systems plc. (Ref: MEIR PhD 16) and the Royal Society (Ref: RGS\R1\191167) are greatly appreciated and acknowledged.

References

- Butt, F.R. and Talha, T., 2019. Numerical investigation of the effect of leading-edge tubercles on propeller performance. *Journal of Aircraft*, 56(3), pp.1014-1028.
- Carlton, J., 2018. *Marine propellers and propulsion*. Butterworth-Heinemann.

- Celik, I.B., Ghia, U., Roache, P.J. and Freitas, C.J., 2008. Procedure for estimation and reporting of uncertainty due to discretization in CFD applications. *Journal of fluids Engineering-Transactions of the ASME*, 130(7).
- Guilmineau, E., Deng, G.B., Leroyer, A., Queutey, P., Visonneau, M. and Wackers, J., 2014, July. Wake simulation of a marine propeller. In 11th World Congress on computational mechanics.
- Hansen, K., Kelso, R. and Doolan, C., 2012. Reduction of flow induced airfoil tonal noise using leading edge sinusoidal modifications. *Acoustics Australia*, 40(3), pp.172-177.
- Hansen, K.L., Kelso, R.M. and Dally, B.B., 2011. Performance variations of leading-edge tubercles for distinct airfoil profiles. *AIAA journal*, 49(1), pp.185-194.
- Ibrahim, I.H. and New, T.H., 2015, June. Tubercle modifications in marine propeller blades. In 10th Pacific Symposium on Flow Visualization and Image Processing (pp. 1-11). Naples Italy.
- Ibrahim, M., Alsultan, A., Shen, S. and Amano, R.S., 2015. Advances in horizontal axis wind turbine blade designs: introduction of slots and tubercle. *Journal of Energy Resources Technology*, 137(5).
- ITTC., 1999. ITTC–recommended procedures-performance, propulsion 1978 ITTC performance prediction method. In International Towing Tank Conference (pp. 7-5).
- ITTC., 2014. ITTC – Recommended Procedures and Guidelines
- Johari, H., Henoch, C., Custodio, D. and Levshin, A., 2007. Effects of leading-edge protuberances on airfoil performance. *AIAA journal*, 45(11), pp.2634-2642.
- Miklosovic, D.S., Murray, M.M., Howle, L.E. and Fish, F.E., 2004. Leading-edge tubercles delay stall on humpback whale (*Megaptera novaeangliae*) flippers. *Physics of fluids*, 16(5), pp.L39-L42.
- Miller, W. and Grzybowski, P, 2007. CTO - Technical Report
- Reissner, H., 1937. On the vortex theory of the screw propeller. *Journal of the Aeronautical Sciences*, 5(1), pp.1-7.
- Richardson, L.F., 1911. IX. The approximate arithmetical solution by finite differences of physical problems involving differential equations, with an application to the stresses in a

masonry dam. *Philosophical Transactions of the Royal Society of London. Series A, Containing Papers of a Mathematical or Physical Character*, 210(459-470), pp.307-357.

Roache, P.J., 1998. Verification of codes and calculations. *AIAA journal*, 36(5), pp.696-702.

Sezen, S., Atlar, M., Fitzsimmons, P., Sasaki, N., Tani, G., Yilmaz, N. and Aktas, B., 2020. Numerical cavitation noise prediction of a benchmark research vessel propeller. *Ocean Engineering*, 211, p.107549.

Shi, W., Rosli, R., Atlar, M., Norman, R., Wang, D. and Yang, W., 2016. Hydrodynamic performance evaluation of a tidal turbine with leading-edge tubercles. *Ocean Engineering*, 117, pp.246-253.

Shi, W., 2017. Biomimetic improvement of hydrodynamic performance of horizontal axis tidal turbines (Doctoral dissertation, Newcastle University).

Shi, W., Atlar, M. and Norman, R., 2017. Detailed flow measurement of the field around tidal turbines with and without biomimetic leading-edge tubercles. *Renewable Energy*, 111, pp.688-707.

Siemens, 2018. STAR CCM+ User Guide

Stanway, M.J., 2008. Hydrodynamic effects of leading-edge tubercles on control surfaces and in flapping foil propulsion (Masters Thesis, Massachusetts Institute of Technology).

Stark, C. and Shi, W., 2021a, June. The influence of leading-edge tubercles on the sheet cavitation development of a benchmark marine propeller. In *40th International Conference on Ocean, Offshore and Arctic Engineering: OMAE 2021*.

Stark, C. and Shi, W., 2021b, June. The influence of leading-edge tubercles on the hydrodynamic performance and propeller wake flow development of a ducted propeller. In *The 31st (2021) International Ocean and Polar Engineering Conference: ISOPE-2021*.

Troll, M.M., Shi, W. and Stark, C., 2021, June. The influence of leading-edge tubercles on wake flow dynamics of a marine rudder. In *9th International Conference on Computational Methods in Marine Engineering: MARINE 2021*.

Watts, P. and Fish, F.E., 2001, August. The influence of passive, leading edge tubercles on wing performance. In *Proc 12th Internat Symp Unmanned Untethered Submersible Tech*. Durham, NH: Autonomous Undersea Systems Institute.

Weber, P.W., Howle, L.E., Murray, M.M. and Miklosovic, D.S., 2011. Computational evaluation of the performance of lifting surfaces with leading-edge protuberances. *Journal of Aircraft*, 48(2), pp.591-600.

Weber, P.W., Howle, L.E. and Murray, M.M., 2010. Lift, drag, and cavitation onset on rudders with leading-edge tubercles. *Marine technology*, 47(1), pp.27-36.

Wei, Z., New, T.H. and Cui, Y.D., 2015. An experimental study on flow separation control of hydrofoils with leading-edge tubercles at low Reynolds number. *Ocean Engineering*, 108, pp.336-349.

Tables

Table 1 Baseline duct and propeller parameters

Variable (Duct)	Unit	Variable (Propeller)	Unit
Type	19A	Type	Kaplan
Outer Diameter, D_d	0.306m	Blade number	4
Inner diameter, D_i	0.254m	Expanded Area Ratio (EAR)	0.55
Chord, L_{DUCT}	0.125m	Pitch-diameter Ratio (P/D)	1
		Diameter, D	0.25m
		Tip Clearance, t	2mm
		Position wrt Duct	$0.5L_{DUCT}$

Table 2 Ducts investigated for geometric optimisation

Model	Label	Tubercle Count	Wavelength, λ	Amplitude, A
1a	Ref	-	-	-
2a	5A 10F	10	94.13mm ($0.75L_{DUCT}$)	5mm ($0.04L_{DUCT}$)
3a	5A 16F	16	58.8mm ($0.47L_{DUCT}$)	5mm ($0.04L_{DUCT}$)
4a	5A 20F	20	47.1mm ($0.38L_{DUCT}$)	5mm ($0.04L_{DUCT}$)
5a	7.5A 10F	10	94.13mm ($0.75L_{DUCT}$)	7.5mm ($0.06L_{DUCT}$)
6a	7.5A 16F	16	58.8mm ($0.47L_{DUCT}$)	7.5mm ($0.06L_{DUCT}$)
7a	7.5A 20F	20	47.1mm ($0.38L_{DUCT}$)	7.5mm ($0.06L_{DUCT}$)
8a	10A 10F	10	94.13mm ($0.75L_{DUCT}$)	10mm ($0.08L_{DUCT}$)
9a	10A 16F	16	58.8mm ($0.47L_{DUCT}$)	10mm ($0.08L_{DUCT}$)
10a	10A 20F	20	47.1mm ($0.38L_{DUCT}$)	10mm ($0.08L_{DUCT}$)

Table 3 Reynolds number calculated for each operating condition

Operating Condition (J)	Advance Velocity (V_A) m/s	Rotation rate (n) RPS	Reynolds Number (Re)
0.001	0.00375	15	1.33E+06
0.1	0.375		1.33E+06
0.2	0.75		1.33E+06
0.3	1.125		1.33E+06
0.4	1.5		1.33E+06
0.5	1.875		1.33E+06
0.55	2.0625		1.34E+06
0.6	2.25		1.34E+06
0.7	2.625		1.34E+06

Table 4 Virtual disk parameters

Parameter	Variable
Inner Radius, R_H	0.019m
Outer Radius R_T	0.125m
Thickness, Δ	0.01m
Position	$0.5L_{DUCT}$
Rotation Rate, n	15rps
Handedness	Right-handed

Table 5 Uncertainty results at $J=0.55$ using BFP and propeller resolved method

		φ_1	φ_2	φ_3	R	%GCI _{FINE}
BFP Method	K_{TD}	0.0262	0.0263	0.0267	0.189	0.54
Propeller Resolved Method	K_{TT}	0.178	0.177	0.172	0.13	0.23
	$10K_Q$	0.279	0.278	0.276	0.33	0.83

Table 6 Tubercle geometrical parameter optimisation data

Label	J	K_{TD}	ETA	C_t
Ref	0.001 (Bollard Pull)	0.2278	1.9956E-03	1.186E+06
5A_10F		0.2362	2.0317E-03	1.207E+06
5A_16F		0.2298	2.0043E-03	1.191E+06
5A_20F		0.2243	1.9807E-03	1.177E+06
7.5A_10F		0.2205	1.9646E-03	1.167E+06
7.5A_16F		0.2141	1.9372E-03	1.151E+06
7.5A_20F		0.2102	1.9203E-03	1.141E+06
10A_10F		0.2085	1.9129E-03	1.136E+06
10A_16F		0.2009	1.8803E-03	1.117E+06
10A_20F		0.1942	1.8515E-03	1.100E+06
Ref	0.55 (Optimum Efficiency)	0.0262	0.604	1.56
5A_10F		0.0246	0.598	1.55
5A_16F		0.0241	0.597	1.54
5A_20F		0.0248	0.599	1.55
7.5A_10F		0.0239	0.596	1.54
7.5A_16F		0.0241	0.597	1.54
7.5A_20F		0.0243	0.598	1.54
10A_10F		0.0239	0.596	1.54
10A_16F		0.0242	0.597	1.54
10A_20F		0.0246	0.598	1.55

Table 7 Regression analysis uncoded coefficients at $J = 0.001$

Term	Coef	SE Coef	T-Value	P-Value	VIF
Constant	0.224789	0.000506	444.31	0.000	
A/c	-0.03284	0.00209	-15.74	0.000	20.56
λ/c	0.02306	0.00216	10.67	0.000	21.45
A/c*A/c	0.00293	0.00208	1.41	0.232	11.20
$\lambda/c*\lambda/c$	-0.01208	0.00224	-5.38	0.006	15.24
A/c*λ/c	0.00234	0.00155	1.51	0.205	4.81

Table 8 Regression analysis model summary at $J = 0.001$

S	R -sq	R -sq(adj)
0.0008640	99.82%	99.59%

Table 9 Regression analysis uncoded coefficients at $J = 0.55$

Term	Coef	SE Coef	T-Value	P-Value	VIF
Constant	0.024449	0.000124	197.55	0.000	
A/c	-0.000461	0.000510	-0.90	0.418	20.56
λ/c	-0.000764	0.000528	-1.45	0.222	21.45
A/c*A/c	0.000567	0.000509	1.11	0.328	11.20
$\lambda/c*\lambda/c$	0.000810	0.000549	1.48	0.214	15.24

$A/c*\lambda/c$	-0.000848	0.000378	-2.24	0.088	4.81
-----------------	-----------	----------	-------	-------	------

Table 10 Regression analysis model summary at $J = 0.55$

S	$R-sq$	$R-sq(adj)$
0.0002113	95.72%	90.36%

Figures

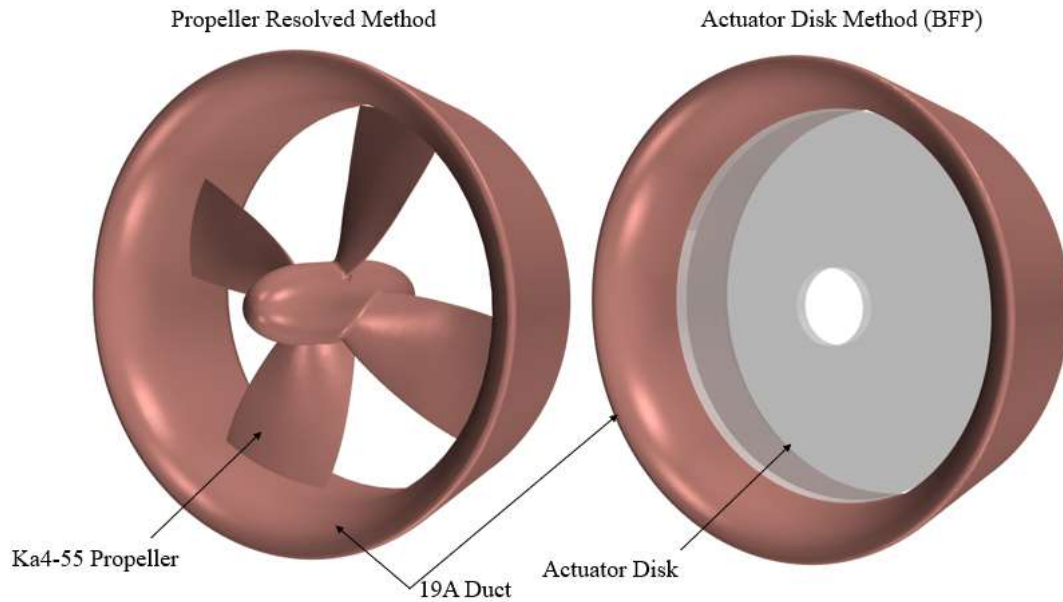


Figure 1 3D model of KA4-55 and 19A duct combination used in propeller resolved (left) and actuator disk (right) methodologies (Carlton, 2018)

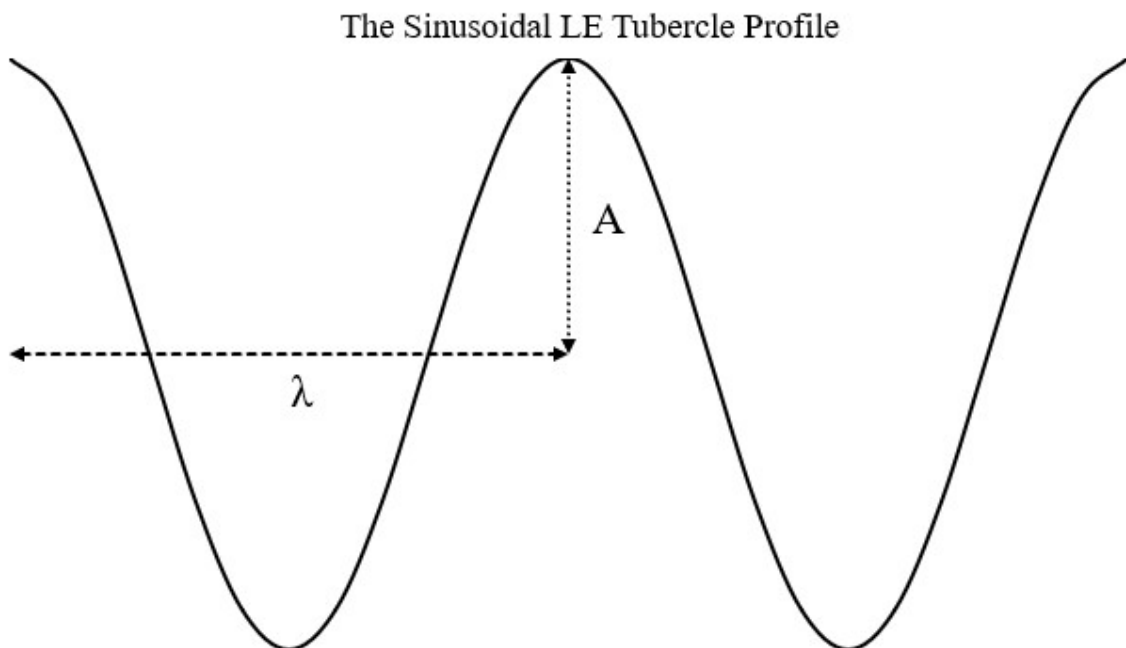


Figure 2 Illustration of the SLE modifications implemented

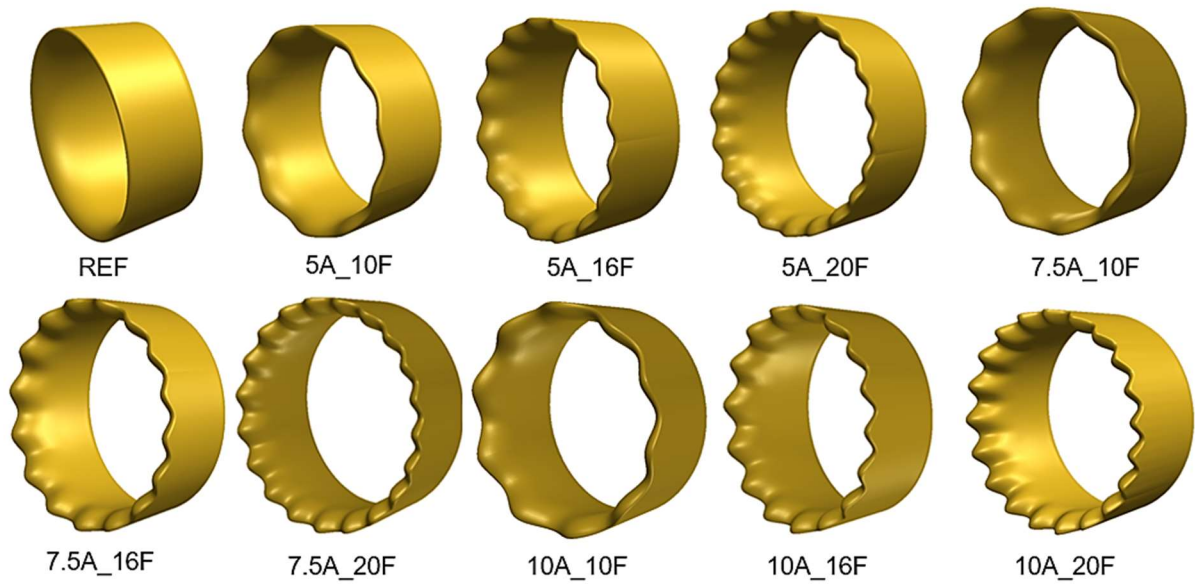


Figure 3 Duct models created for tubercle geometrical parameter optimisation

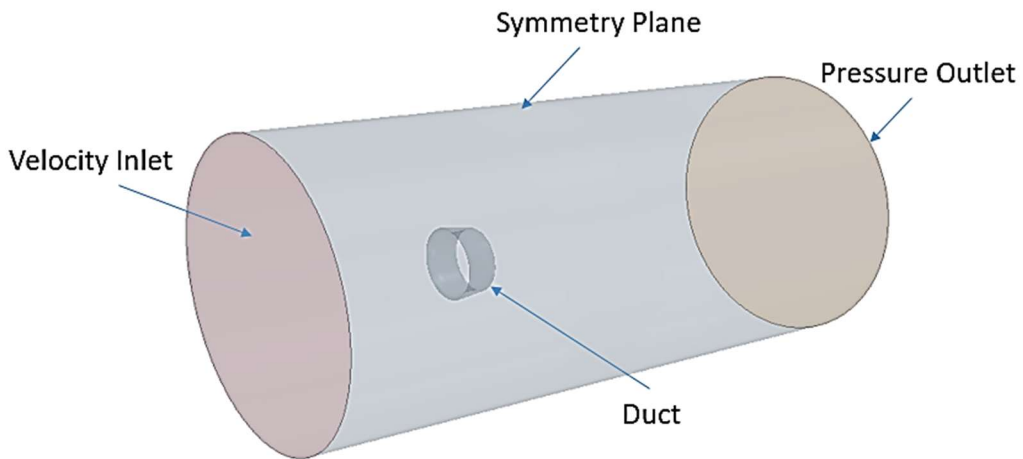


Figure 4 The computational domain using BFP method

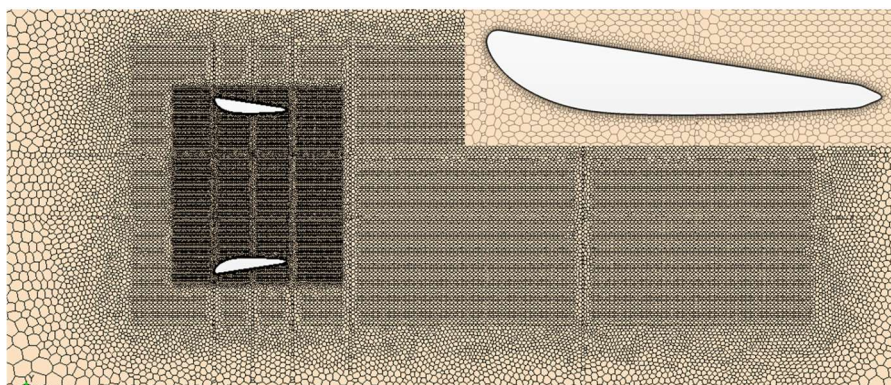


Figure 5 A section view of the grid around the propeller duct and zoomed in view of the boundary layer using BFP method



Figure 6 Reference duct surface mesh used in the BFP method

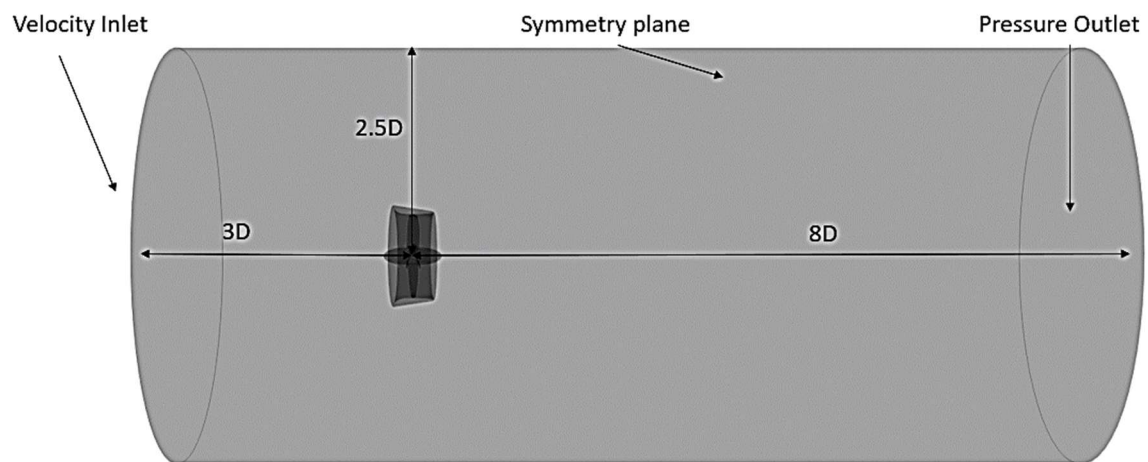


Figure 7 The computational domain using the propeller resolved method

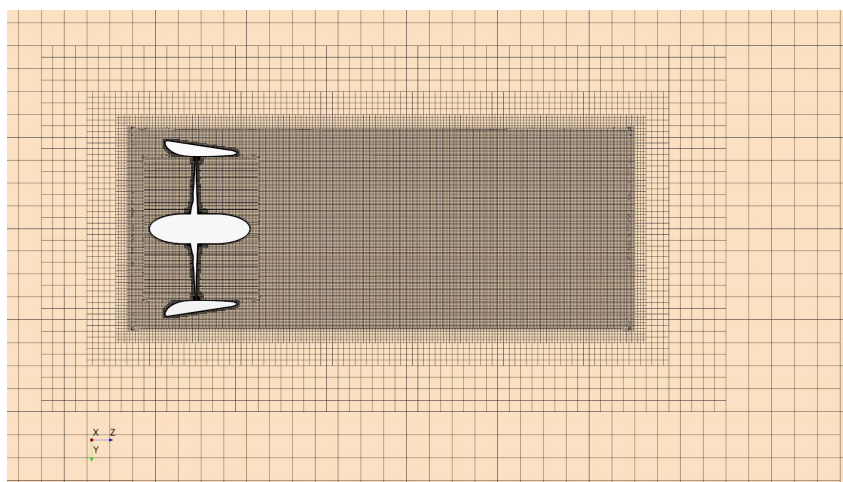


Figure 8 Cut plane of volume mesh used in the propeller resolved method



Figure 9 Surface mesh of KA455 + 19A duct used in the propeller resolved method

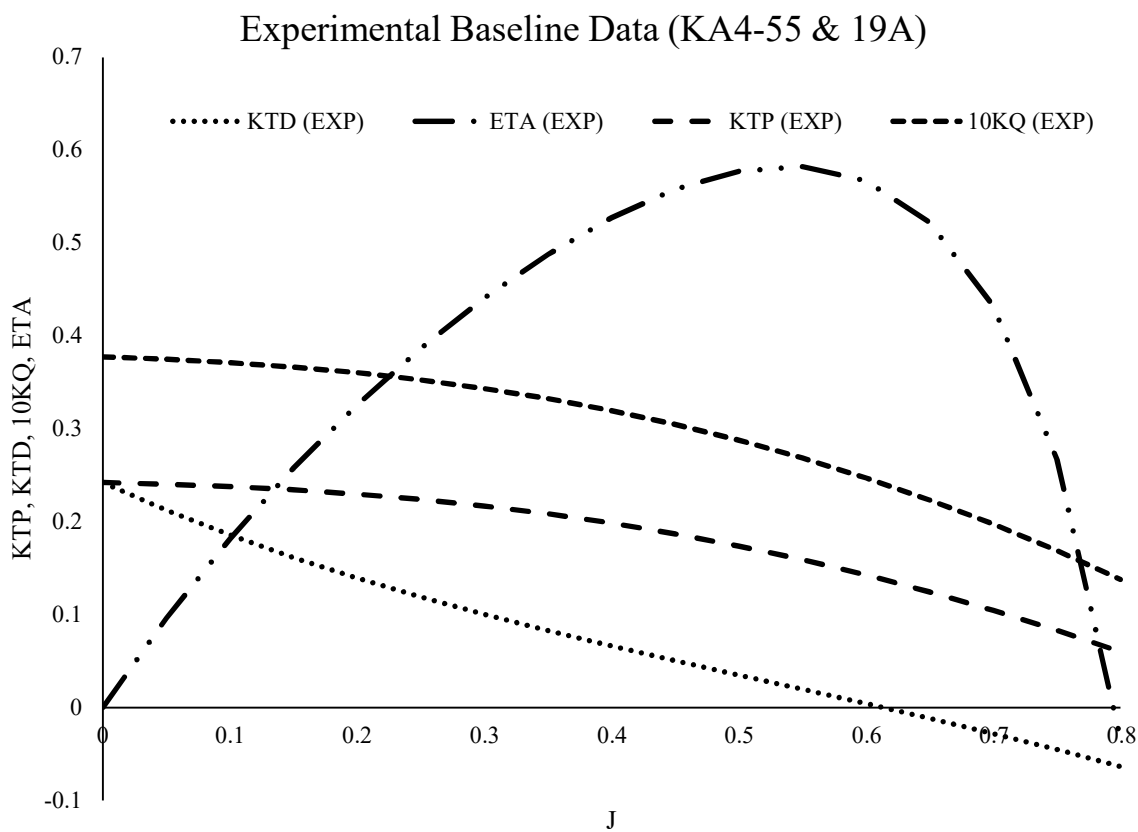


Figure 10 Experimental open water characteristics for KA4-55 and 19A (Miller and Grzybowski, 2007)

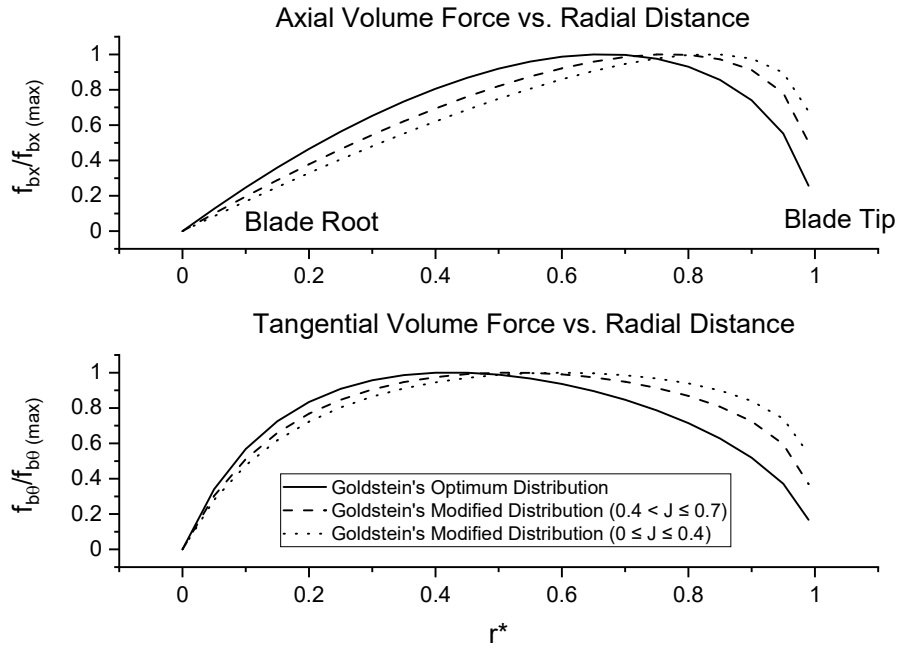


Figure 11 Goldstein's Optimum and Modified Distribution

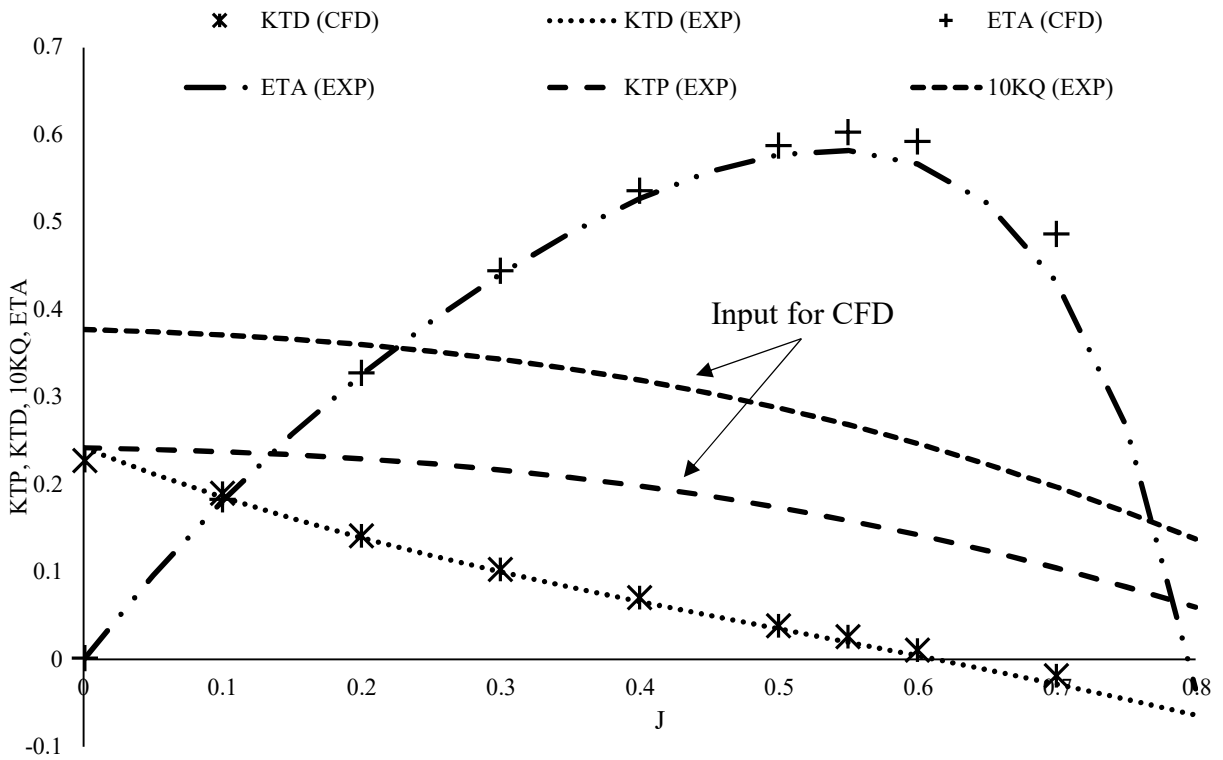


Figure 12 Comparison with experimental results using the BFP method

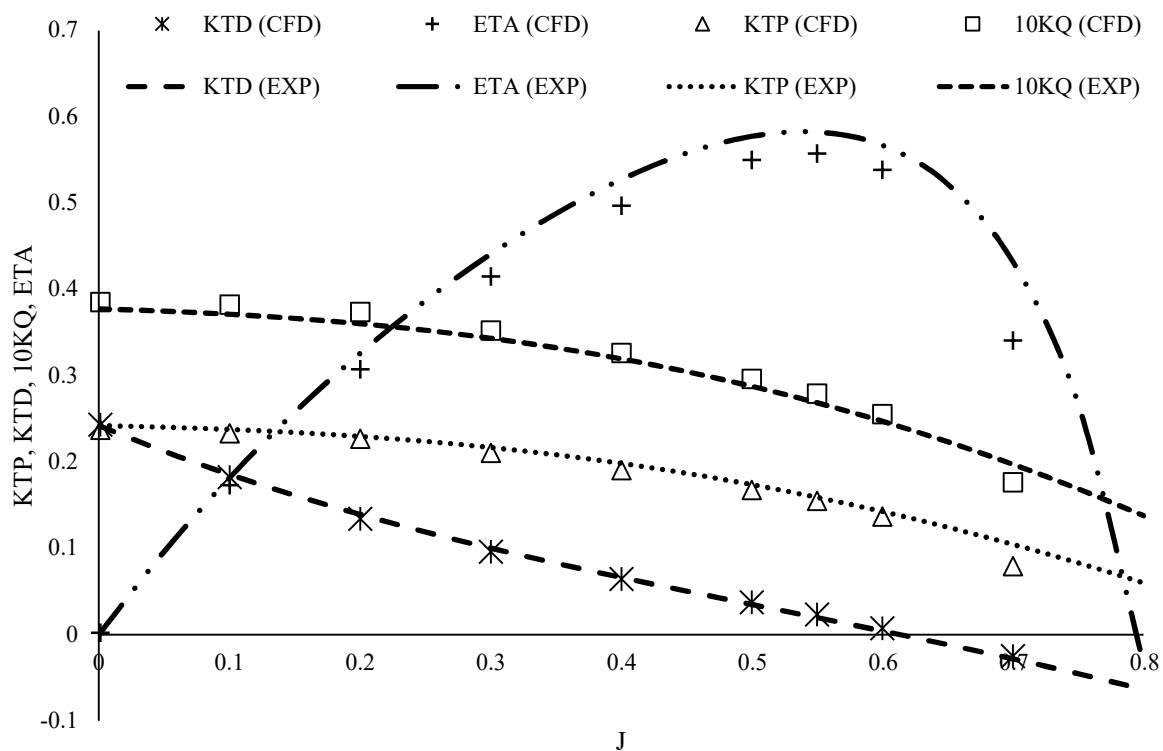


Figure 13 Comparison with experimental results using the propeller resolved method

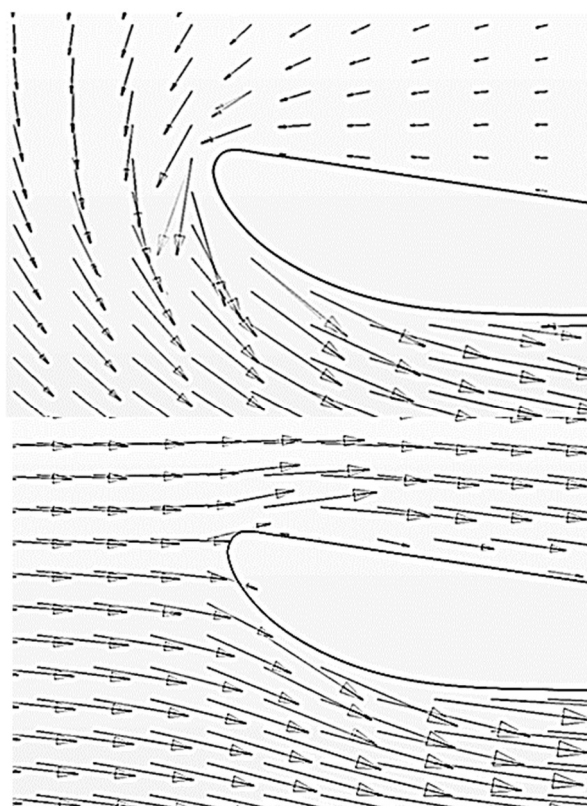


Figure 14 Induced inflow angle for $J = 0.001$ (top) and 0.55 (bottom), showing variation in inflow angle

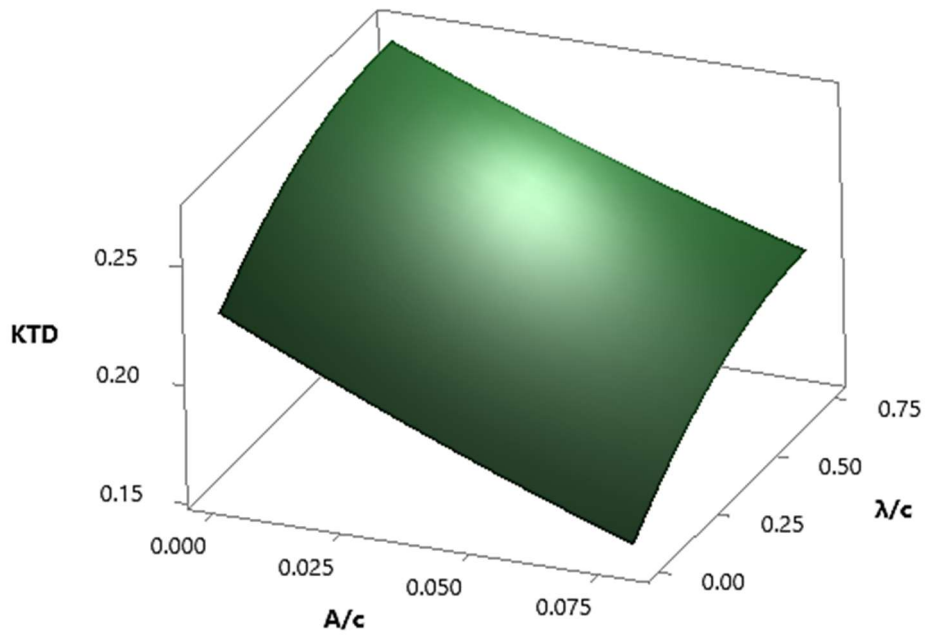


Figure 15 Surface optimisation plot at $J = 0.001$

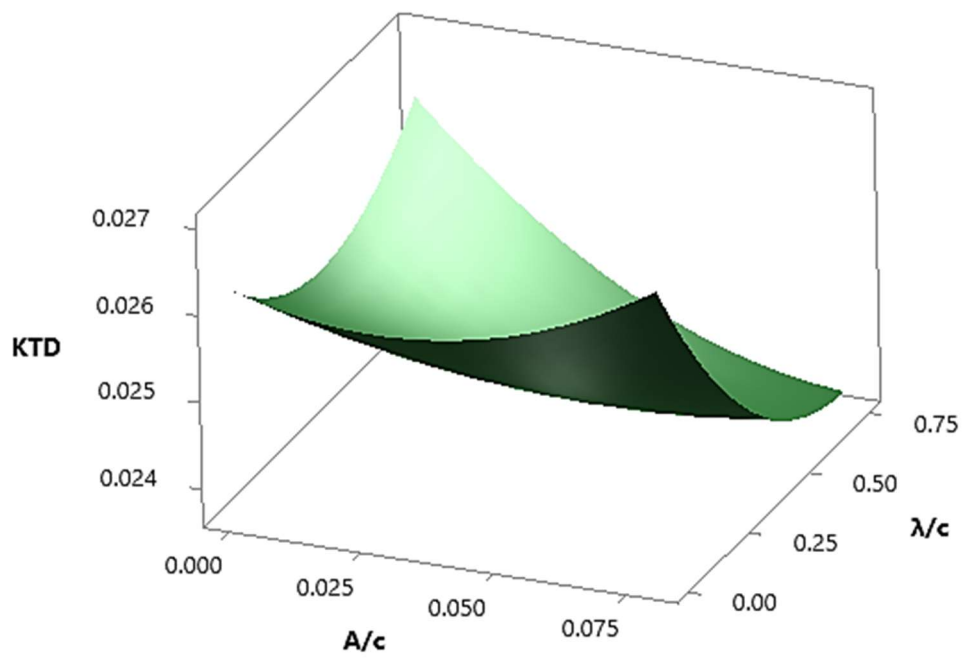


Figure 16 Surface optimisation plot at $J = 0.55$

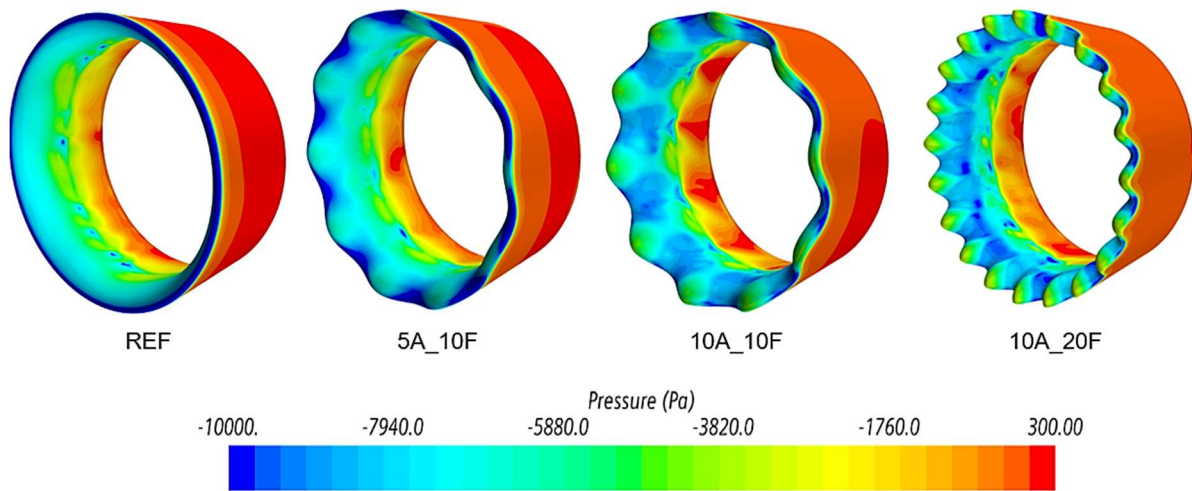


Figure 17 Pressure distribution on duct surface at $J = 0.001$

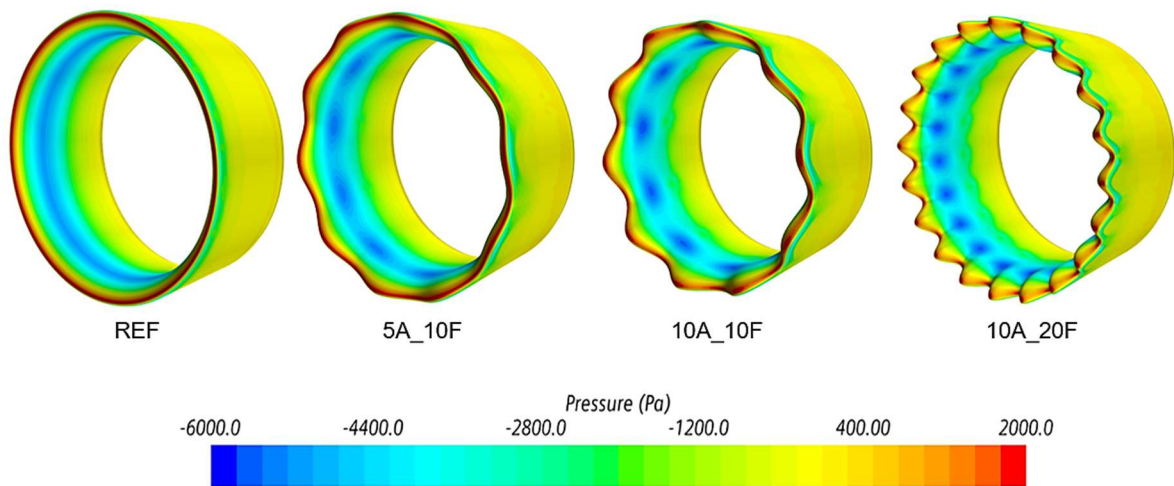


Figure 18 Pressure distribution on duct surface at $J = 0.55$

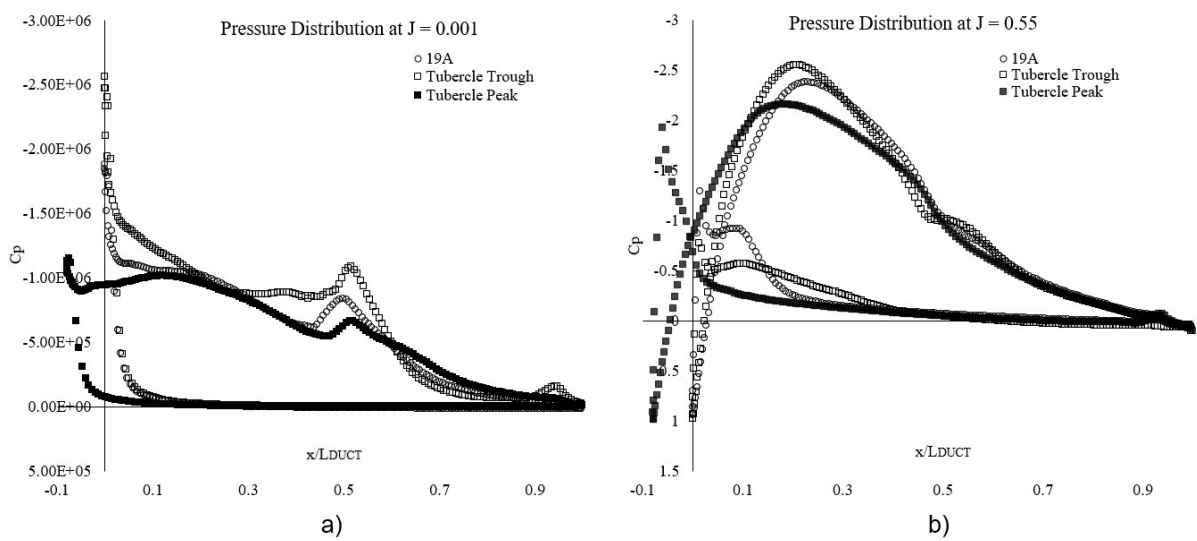


Figure 19 2D static pressure coefficient plots for REF and SLE (5A_10F) duct

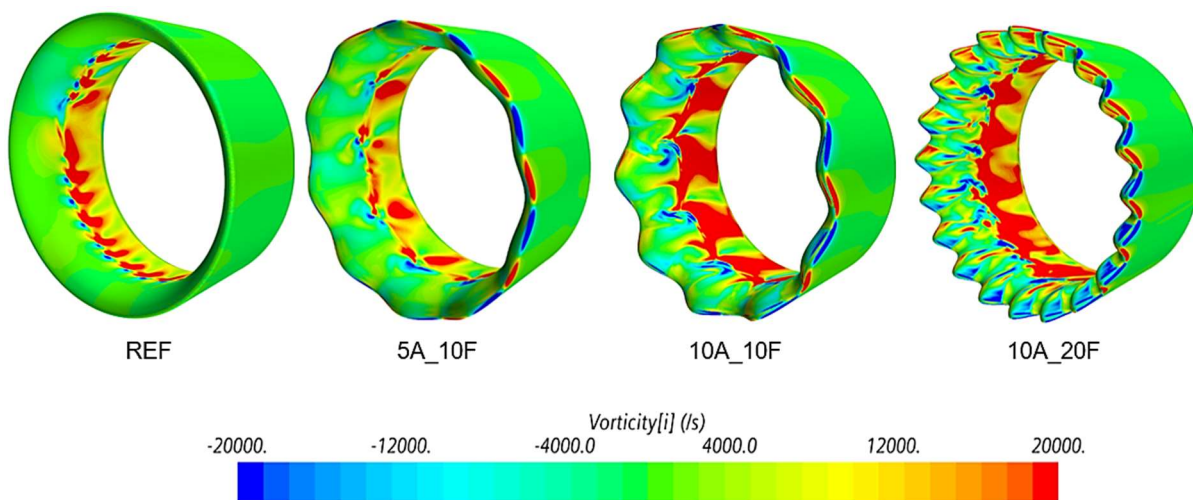


Figure 20 SLE ducts with varying amplitude and wavelength, streamwise vorticity on the duct surface at $J = 0.001$

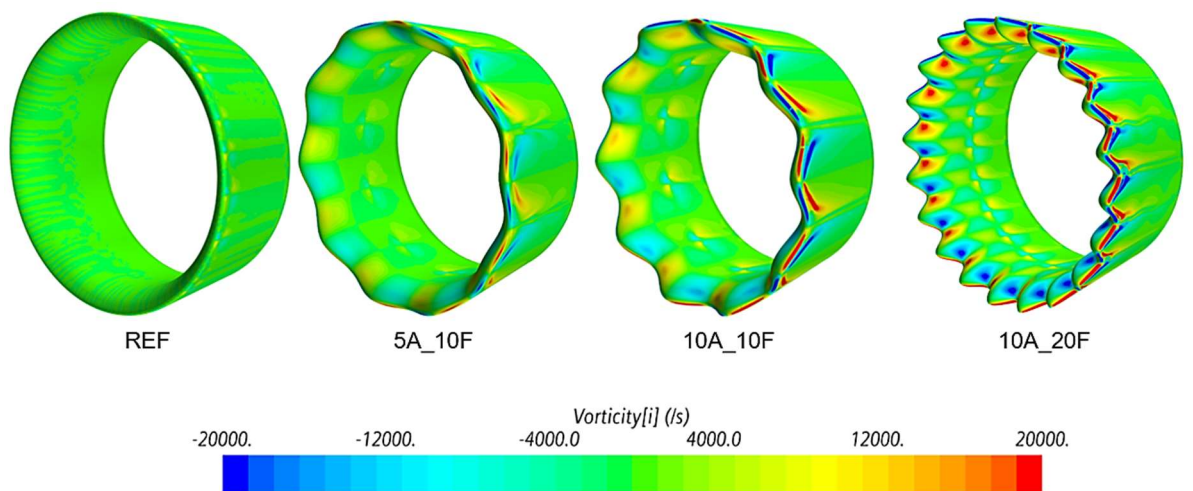


Figure 21 SLE ducts with varying amplitude and wavelength, streamwise vorticity on the duct surface at $J = 0.55$

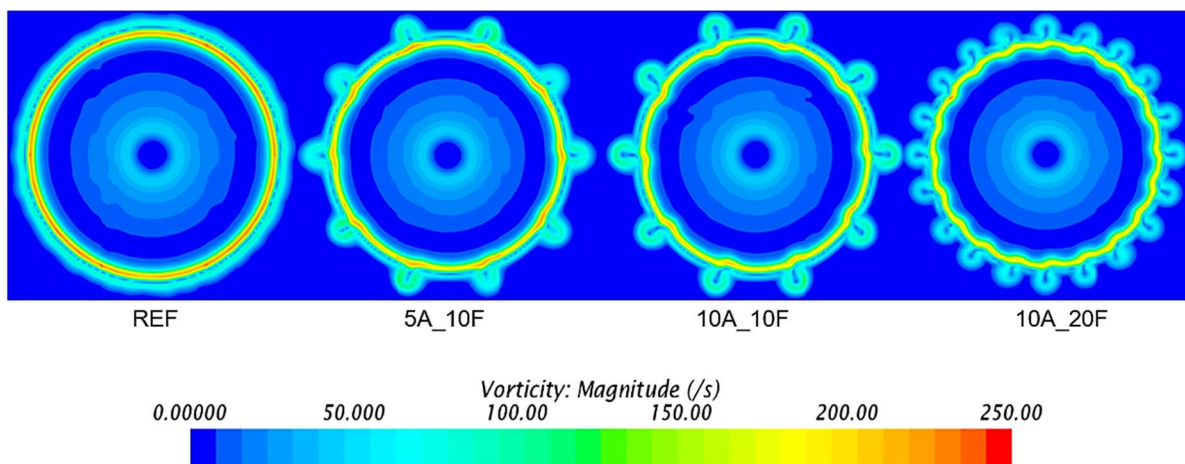


Figure 22 SLE tubercle ducts 5A_10F, 10A_10F and 10A_20F vorticity magnitude at $X/D = 0.6$ and $J = 0.55$

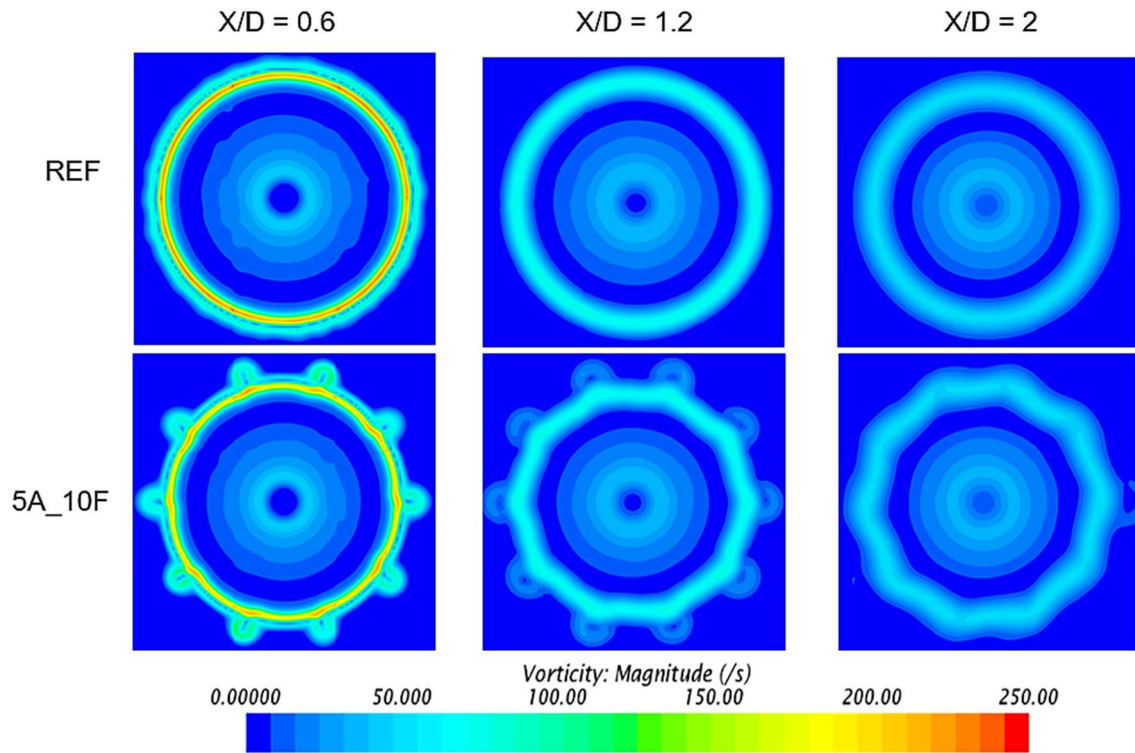


Figure 23 Reference and modified (5A_10F) ducts vorticity magnitude at $X/D=0.6, 1.2$ and 2 for $J = 0.55$

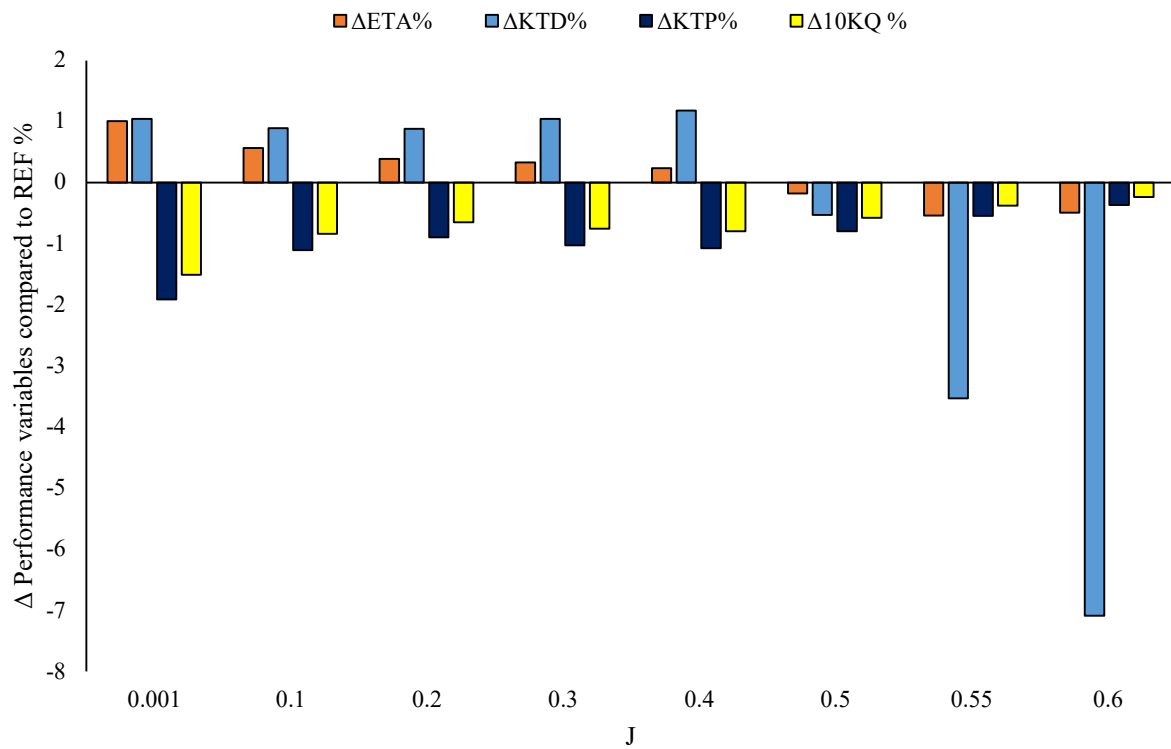


Figure 24 Percentage difference in performance variables due to the inclusion of LE tubercles SLE, 5A_10F using the propeller resolved method

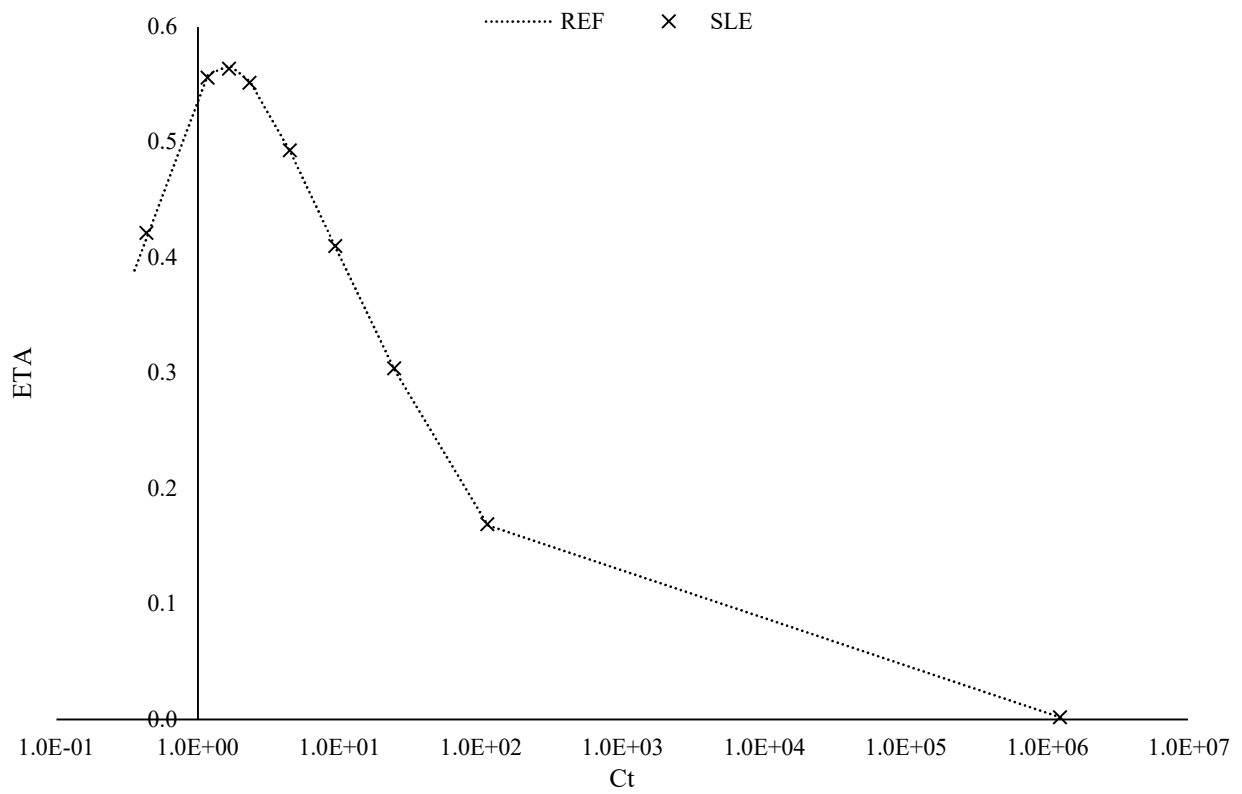


Figure 25 ETA vs Ct for REF and SLE ducted propeller combinations

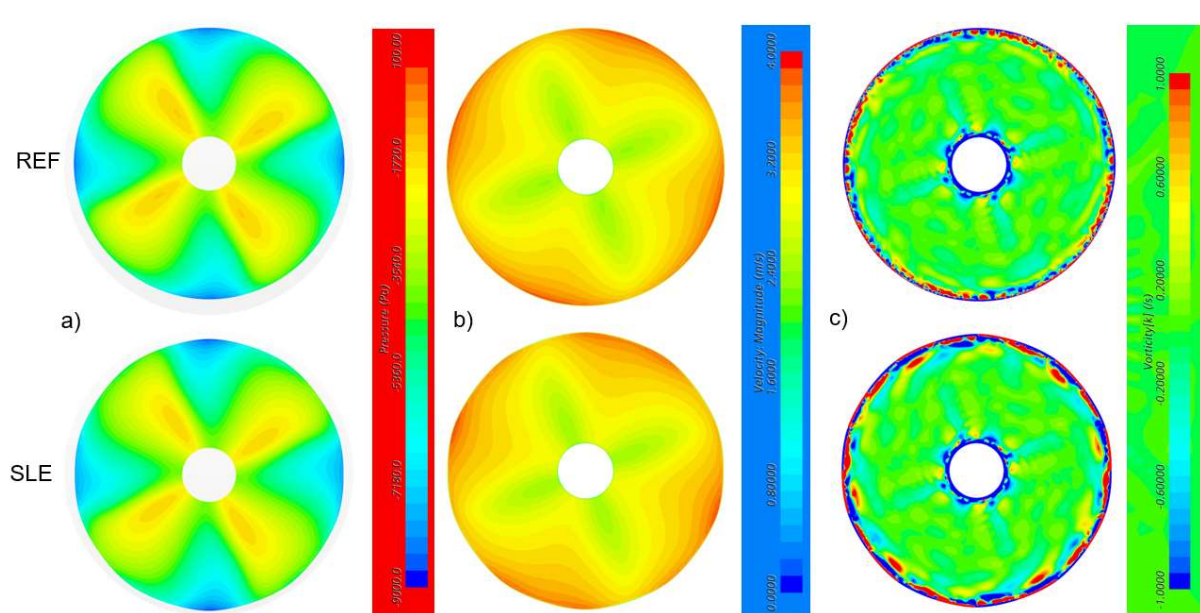


Figure 26 Inflow a) pressure, b) velocity and c) streamwise vorticity distributions of REF and SLE ducted propeller combinations at $J = 0.3$

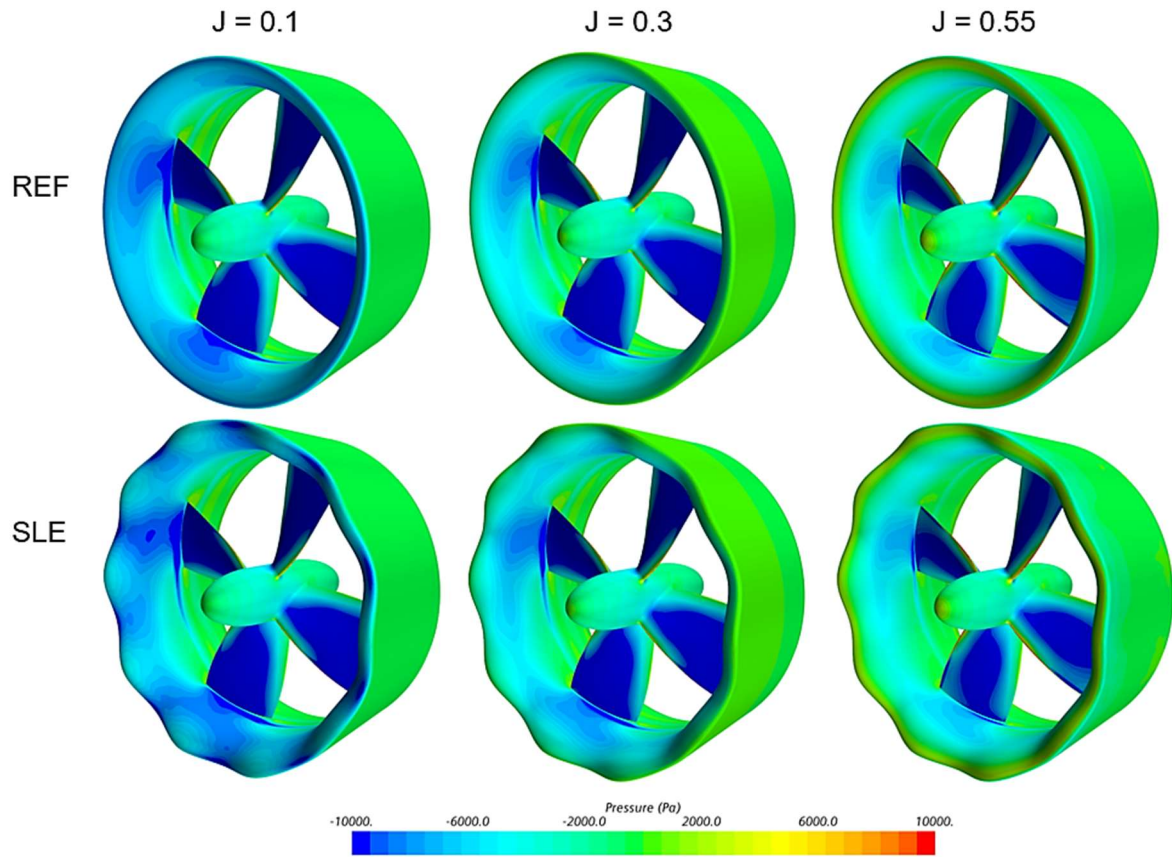


Figure 27 Surface pressure distributions (propeller suction side) of REF and SLE ducted propellers at $J= 0.1, 0.3$ and 0.55

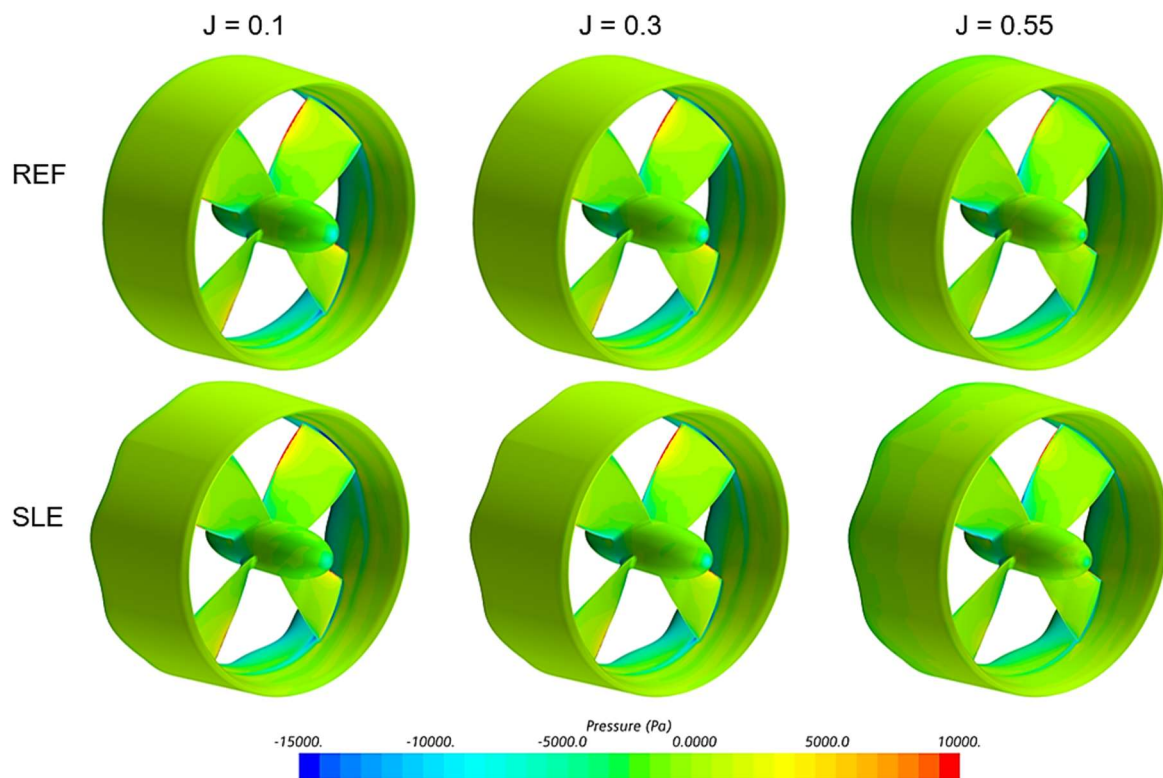


Figure 28 Surface pressure distributions (propeller pressure side) of REF and SLE ducted propellers at $J= 0.1, 0.3$ and 0.55

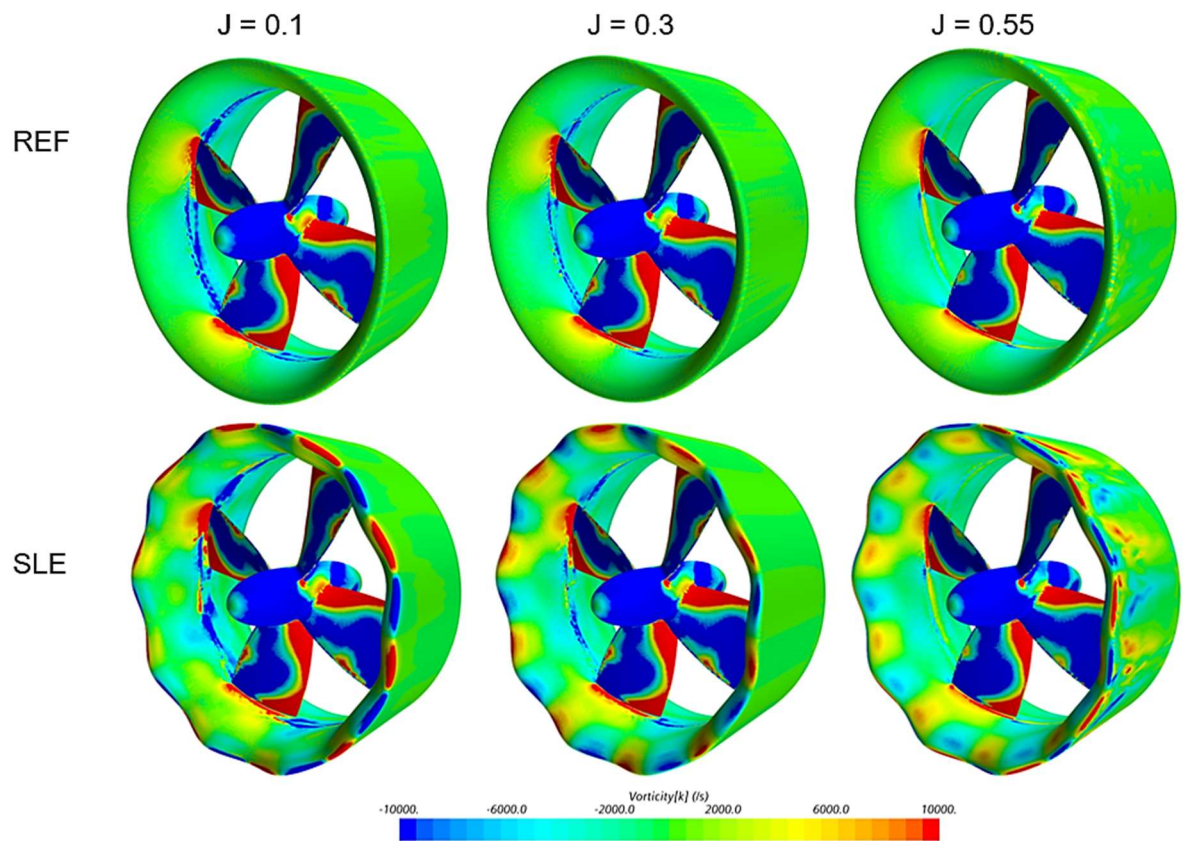


Figure 29 Surface streamwise vorticity distributions of REF and SLE (5A_10F) ducts at J= 0.1, 0.3 and 0.55

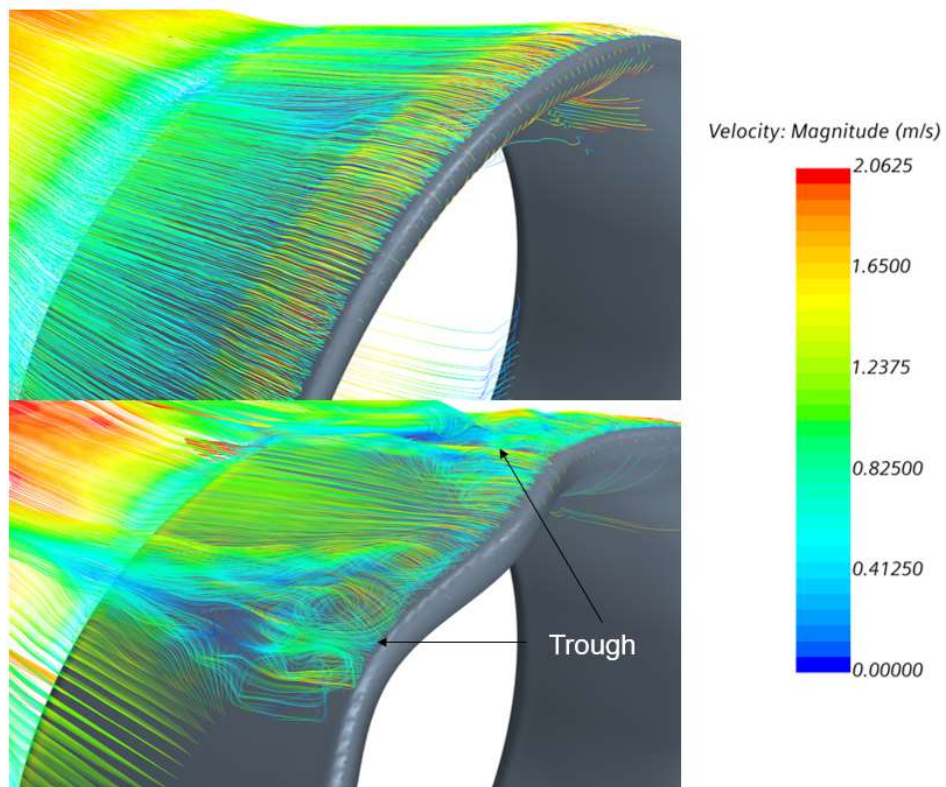


Figure 30 Velocity streamlines for REF and SLE duct at $J = 0.55$